Earth and Space Science

RESEARCH ARTICLE
10.1029/2020EA001293

Key Points:

- Measurements of horizontal wind gradients at low-latitude mesosphere and lower thermosphere altitudes
- These gradients of the horizontal winds show strong temporal and altitude variability that are not observed at high latitudes
- Improved vertical winds are obtained using a gradient wind field method inherently free from horizontal divergence contamination

Supporting Information:

- Supporting Information S1

Correspondence to:
J. L. Chau,
chau@iap-kborn.de

Citation:
Chau, J. L., Urco, J. M., Vierinen, J., Harding, B. J., Clahsen, M., Pfeffer, N., et al. (2021). Multistatic specular meteor radar network in Peru: System description and initial results. *Earth and Space Science*, *8*, e2020EA001293. https://doi.org/10.1029/2020EA001293

Received 8 JUN 2020
Accepted 22 NOV 2020

© 2020. The Authors.
This is an open access article under the terms of the Creative Commons Attribution-NonCommercial License, which permits use, distribution and reproduction in any medium, provided the original work is properly cited and is not used for commercial purposes.

Multistatic Specular Meteor Radar Network in Peru: System Description and Initial Results

J. L. Chau[1], J. M. Urco[1,2], J. Vierinen[3], B. J. Harding[4], M. Clahsen[1], N. Pfeffer[1], K. M. Kuyeng[5], M. A. Milla[5], and P. J. Erickson[6]

[1]Leibniz Institute of Atmospheric Physics at the University of Rostock, Kühlungsborn, Germany, [2]Department of Electrical and Computer Engineering and Coordinated Science Laboratory, University of Illinois at Urbana-Champaign, Urbana, IL, USA, [3]The Arctic University of Norway, Tromso, Norway, [4]Space Sciences Laboratory, University of California, Berkeley, Berkeley, CA, USA, [5]Radio Observatorio de Jicamarca, Instituto Geosfísico del Perú, Lima, Peru, [6]MIT Haystack Observatory, Westford, MA, USA

Abstract The mesosphere and lower thermosphere (MLT) region is dominated globally by dynamics at various scales: planetary waves, tides, gravity waves, and stratified turbulence. The latter two can coexist and be significant at horizontal scales less than 500 km, scales that are difficult to measure. This study presents a recently deployed multistatic specular meteor radar system, SIMONe Peru, which can be used to observe these scales. The radars are positioned at and around the Jicamarca Radio Observatory, which is located at the magnetic equator. Besides presenting preliminary results of typically reported large-scale features, like the dominant diurnal tide at low latitudes, we show results on selected days of spatially and temporally resolved winds obtained with two methods based on: (a) estimation of mean wind and their gradients (gradient method), and (b) an inverse theory with Tikhonov regularization (regularized wind field inversion method). The gradient method allows improved MLT vertical velocities and, for the first time, low-latitude wind field parameters such as horizontal divergence and relative vorticity. The regularized wind field inversion method allows the estimation of spatial structure within the observed area and has the potential to outperform the gradient method, in particular when more detections are available or when fine adaptive tuning of the regularization factor is done. SIMONe Peru adds important information at low latitudes to currently scarce MLT continuous observing capabilities. Results contribute to studies of the MLT dynamics at different scales inherently connected to lower atmospheric forcing and E-region dynamo related ionospheric variability.

Plain Language Summary The mesosphere and lower thermosphere (MLT) region is dominated by neutral wind dynamics with structure scales ranging from a few thousands of kilometers down to a few kilometers. In this work, we present a new state-of-the-art ground-based radar system using multistatic meteor scattering that allows tomographic studies of MLT wind dynamics at scales not possible before. Given the location of the radar network at the magnetic equator, its focus is on wind dynamics peculiar to equatorial latitudes. Two methods for estimating the mesospheric neutral wind field are used. One takes into account wind gradients in addition to mean wind (gradient method). The other estimates a spatially resolved wind vector field and uses an additional mathematical constraint that produces smooth wind field solutions (regularized wind field inversion method). Using the gradient method, the vertical wind estimate is improved. For the first time at MLT equatorial latitudes, parameters familiar to meteorologists, such as horizontal divergence and relative vorticity are obtained. Measurements from this new system have the potential to contribute to coupling studies of the atmosphere and the ionosphere at low latitudes.

1. Introduction

The mesosphere and lower thermosphere (MLT) region between 60 and 110 km forms the boundary between the lower atmosphere and space. This region is dominated by atmospheric dynamics including planetary waves, tides, gravity waves, and stratified turbulence. The main sources of these dynamics lie mainly in the lower atmosphere. Similarly, neutral dynamics and electrodynamics at higher altitudes can be modified by locally generated MLT dynamics or by perturbations propagating from below and interacting with the MLT region (e.g., Vincent, 2015, and references therein).

MLT large scale dynamics, either from wind or temperature measurements, have been extensively studied in the last two decades with ground- and satellite-based instruments and with general circulation models (GCMs). There has been significant progress in the understanding of these dynamics particularly in their mean flows, planetary waves, and tidal parameters (Pancheva & Mukhtarov, 2011; Vincent, 2015). For example, it is well known that semidiurnal tides dominate at mid and high latitudes, while at low latitudes, diurnal tides are more important (e.g., Smith, 2012).

In addition to dominant MLT diurnal tides at low latitudes (e.g., Davis et al., 2013), other salient MLT large scale dynamics peculiar to low latitudes occur: ultrafast Kelvin waves with periods of 3–4 days, quasi-two-day waves, the mesospheric semiannual oscillation (MSAO), and the mesospheric quasibiennial enhancement (Abdu et al., 2015; Pancheva & Mukhtarov, 2011; Venkateswara Rao, Tsuda, Riggin, et al., 2012b). Previous observational contributions to these studies from single ground-based stations have been focused on providing excellent time coverage, but they have lacked spatial (wave number) information. Therefore, single-station ground-based observations at low latitudes have usually been complemented with GCMs to complete the spatiotemporal picture (e.g., Davis et al., 2013).

MLT dynamics at low latitudes has been shown to have important influence on ionospheric and thermospheric variability at different scales. For example, large ionospheric perturbations have been associated with sudden stratospheric warming events, which are initiated in the winter polar stratosphere but produce global changes (e.g., Pedatella et al., 2018). Additionally, enhanced ionospheric perturbations associated with lunar tide enhancement have been observed and modeled at low latitudes (e.g., Chau et al., 2009, 2012; Fejer et al., 2010; Goncharenko et al., 2010; Pedatella et al., 2012). Similarly, modulations of *F*-region electron densities around the magnetic equator have been attributed to effects of nonmigrating diurnal tides (England, 2012; Immel et al., 2006). Both of these atmospheric and ionospheric coupling examples at low latitudes are in turn attributed to an imprinting of MLT dynamics through the so-called *E*-region dynamo. Recently, the NASA Ionospheric Connection Explorer (ICON) mission has started operation to study these and other atmospheric and ionospheric coupling processes at low latitudes (e.g., Immel et al., 2018).

Monostatic specular meteor radars (SMRs) have been widely used to study MLT dynamics. These radars are able to measure MLT dynamics from 75 to 105 km continuously by providing horizontal winds averaged on areas of ∼400 km diameter at 1–2 h cadence with 2–4 km altitude resolution. In the case of mid and high latitudes, SMRs from different longitudes at selected mid and high latitude bands have been analyzed together to provide spatial (wavenumber) information on dominant tides and planetary waves (e.g., He et al., 2018; Manson et al., 2009).

In this work, we present the first results from a multistatic SMR installed at and around the Jicamarca Radio Observatory (JRO) in Peru. This system joins a small list of SMRs located at low latitudes, here defined as between ±15° latitude (see Araújo et al., 2014; Davis et al., 2013; Rao et al., 2014; Venkateswara Rao, Tsuda, Riggin, et al., 2012b, for references and results of other low latitude SMRs). All of these previous systems have operated in a monostatic mode, where transmitter and receivers are co-located. Multistatic SMR capabilities from this new system in Peru add considerably to these observational capabilities through studies of large-scale dynamics in combination with other low latitude ground-based radars. In particular, the combination is able to separate space-time observational ambiguities, similar to other studies conducted at mid and high latitudes (He & Chau, 2019; Manson et al., 2009; Murphy et al., 2006).

A multistatic SMR brings the possibility of more scattering detections and pointing diversity through provision of different viewing angles. The former helps to provide standard measurements with better quality, while the latter allows spatial measurements of MLT winds within the illuminated area (Chau et al., 2017; Stober & Chau, 2015). Multistatic capabilities provide attractive, and straightforward, observational products, in particular estimation of the horizontal wind gradients, in a manner similar to previous successful studies of the lower atmosphere and thermosphere (e.g., Browning & Wexler, 1968; Burnside et al., 1981). These horizontal gradients are important for proper estimation of several key MLT parameters. For example, using two links (from two closely located monostatic SMRs), Chau et al. (2017) found that the vertical wind estimate is contaminated by horizontal divergence if horizontal gradients of the horizontal wind are not considered. In addition, they reported the climatology of horizontal divergence and relative vorticity in the Arctic MLT region. Using these horizontal divergence estimates, Laskar et al. (2017) provided

reasonable estimates of mean summer mesospheric vertical winds, using the mass continuity equation and assuming an anelastic flow, that is, incompressible and stratified.

The multistatic SMR results reported here originated in a concept called MMARIA (Multistatic, Multifrequency Agile Investigations of the Atmosphere) (Stober & Chau, 2015) whose primary goal was to add interferometric receivers located with 60–200 km radius from existing transmitters. In this work, we have implemented MMARIA through a project named SIMONe. SIMONe (Spread Spectrum Interferometric Multistatic meteor radar Observing Network) makes use of coded continuous waves (CWs), multiple-input multiple-output (MIMO), and compressed sensing concepts (Urco et al., 2018, 2019; Vierinen et al., 2016). Compared to the original system architecture, SIMONe allows MMARIA implementations to be cheaper and more robust, with easier implementation of additional bistatic links, as only a single receiver antenna is needed for each bistatic receiver station (e.g., Chau et al., 2019).

Beyond implementation specifics and inherent horizontal resolution capability of MLT winds (e.g., Chau et al., 2017; Stober et al., 2018), multistatic SMRs can be also used to improve the estimation of kinetic energy and momentum fluxes at regional scales. In particular, analysis can either estimate average values of these quantities in a manner similar to traditional techniques used in monostatic SMRs (e.g., Hocking, 2005), or further analysis can produce important information on spatiotemporal features using second-order statistics between detections (e.g., Vierinen et al., 2019). The former requires subtraction of large-scale wind contributions (means and tides) to yield values which represent GW contributions (e.g., Andrioli et al., 2013). This approach has been implemented previously in a bistatic configuration in Australia by Spargo et al. (2019), and obtained an increase of precision on momentum flux estimates mainly due to an increased number of detections. The latter method of employing second-order statistics between detections has been implemented with 24 h of data in a special campaign that consisted of 14 bistatic links in northern Germany. Although momentum fluxes were not reported given the relatively short duration of collected data, spatial (3-D) and temporal correlation, structure, and spectral functions were obtained as detailed in Vierinen et al. (2019).

As in the case of mid and high latitudes, measurement of GW momentum fluxes represents one of the most challenging and needed tasks at low latitudes (e.g., Fritts & Alexander, 2003). Not only is this information needed to improve GCMs, but also observations are furthermore key to understanding different MLT processes. For example, Venkateswara Rao, Tsuda, and Kawatani (2012a) reported significant correlations between the strength of MSAO and short-period GW variances at mesospheric altitudes over Indonesia, suggesting that GW momentum deposition drives the MSAO. However, GW momentum flux measurements are still needed to validate this hypothesis.

Our system, SIMONe Peru, represents one of the first two operational multistatic SMRs with MIMO and spread-spectrum technology. The second system has been installed in southern Argentina (SIMONe Argentina). Both system have been running continuously since October 2019. In this work, besides the system description, we present preliminary multistatic SMR results with emphasis on neutral winds.

This study begins by describing in detail a general SIMONe system, followed by the specifics of the SIMONe Peru installation. Three methods for obtaining wind fields are then presented: (1) homogeneous method; (2) gradient method; and (3) a regularized wind field inversion method. MLT wind results for large-scale features are presented for the first 6 months of data, while mesoscale features are shown for selected times in Section 4. Using the spatial information provided by the multistatic method, our analysis places special emphasis on quantifying contamination of vertical wind components by horizontal wind divergence if horizontal gradients are not considered. Observations of other atmospheric and ionospheric targets are presented and discussed in Section 5. Finally, a summary of main results and future plans is presented.

2. System Description

The SIMONe concept was introduced and described by Chau et al. (2019) and later used on a special seven-day campaign in northern Germany (e.g., Vierinen et al., 2019). In both cases, the concept was implemented using hardware and software prototypes. In this section, we describe in detail our most recent

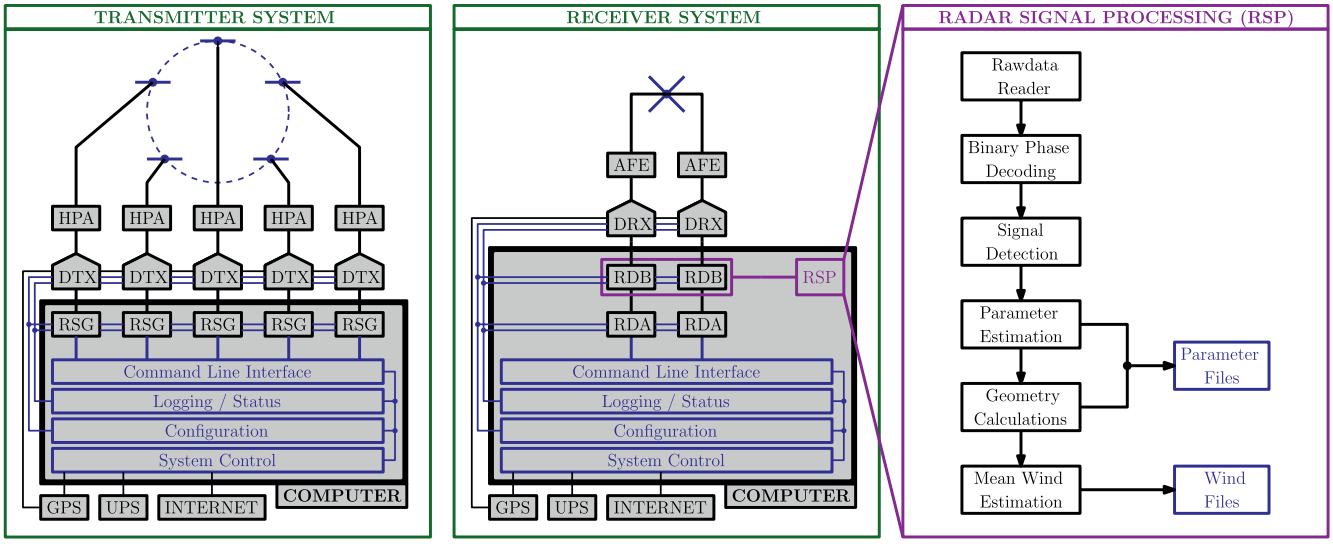

Figure 1. SIMONe system block diagram: (left) transmitter, (middle) receiver, and (right) radar signal processing (RSP).

SIMONe implementation in general and the specifics of SIMONe Peru. A general architectural description is useful since a similar system has also been installed in Argentina (SIMONe Argentina), and two new systems will be installed in northern Germany and northern Norway in the near future.

2.1. A General Description of SIMONe

SIMONe uses modern radar approaches, such as spread spectrum, MIMO, and compressed sensing, to study the MLT region with a multistatic radar configuration. On transmission, multiple antennas (e.g., multiple input) are used in an interferometer configuration of at least five antennas, each of them fed by an independent transmitter. Each transmitter uses coded CW waveforms with a different pseudorandom binary code on each transmitter (e.g., Vierinen et al., 2016). To limit interstation interference, the seeds of the random number generators producing the codes are carefully selected to minimize cross-correlations among all codes.

On reception, a SIMONe station can consist of one antenna or more antennas arranged in an interferometer configuration. The former allows the implementation of MISO link (i.e., Multiple-Input, Single Output). On the other hand, multiple receive antennas allow either a SIMO (Single-Input Multiple Output; one coherent transmit signal) or a MIMO (multiple coherent transmit signals) link. SIMO is the standard configuration of monostatic SMRs, where the angle-of-arrival (AOA) is measured, defined as incoming ray angle with respect to the receiver array. In the case of a MISO configuration, the angle-of-departure (AOD) is measured as the ray angle with respect to the transmitter, while in MIMO configurations, AOAs and AODs are measured simultaneously from the same target (e.g., Chau et al., 2019, for more details).

Figure 1 shows a block diagram of the main components of a typical SIMONe system, arranged as transmitter, receiver, and radar signal processing (RSP). On transmission, we use 450-W CW power amplifiers (HPA) manufactured by Hilberling on each antenna. The digital transmitter unit (DTX) creates HPA driver signals as a low-power phase-modulated CW signal that is generated by a software defined radio unit, currently implemented as a National Instruments USRP N200 with a BasicTX transmitter daughter board. DTX units are commanded with modulating signal information by a radar signal generator (RSG) inside the transmitter computer. The RSG receives user instructions related to waveform, code, baud rate, period, amplitude, and phase. The main computer is connected to the internet for remote control functionality, and to an uninterrupted power supply. A Trimble global position system (GPS) receiver unit provides a globally coherent 10 MHz reference clock and one pulse-per-second (PPS) signal to the DTX for multistatic synchronization, and provides timing information to the computer.

On reception, signals from each antenna are amplified and filtered by an analog front end (AFE). The amplified signals are fed into a Digital Receiver (DRX), implemented as a National Instruments USRP-N200 with a BasicRX receiver daughter board. Signals from two antennas are fed to each DRX. Inside the DRX, the signal is digitized, down-converted to in-phase and quadrature components, and decimated. The digital samples are stored by the receiving computer in a raw data buffer (RDB) and a raw data archive (RDA). Data storage employs MIT Haystack Observatory's Digital RF coherent RF data package (https://github.com/MITHaystack/digital_rf), in which each complex RF voltage level sample is coherently referenced to the Unix time standard (fractional seconds since 0000 UTC 1970-01-01) and recorded in Hierarchical Data Format version 5 (HDF5) with tagged metadata. The RDB stores up to 1 h of data in ring-buffer configuration and is used for real-time processing and monitoring. The RDA stores up to 14 days of data in ring-buffer configuration and this deeper buffer is used for off-line routine analysis or externally triggered processing of special events (e.g., bolides). The receiving computer is connected to the internet for remote control and data transfer. As in the case of the transmitter, a Trimble GPS receiver unit provides a globally coherent 10 MHz reference clock and 1 PPS to the USRP-N200, and timing information to the computer. The precision of the 1 PPS edge is less than 25 ns, while the frequency jitter of the reference clock is a fraction of 1 Hz, providing SIMONe with excellent range synchronization and Doppler capability.

The receiver and transmitter computers run a Linux operating system (Ubuntu distribution). Internet connection depends on system location, but is flexible. For example, we have used a combination of wired internet service provider with either dynamic or static IP address, as well as wireless internet using an available cellular phone company.

The RSP modules have been developed in the Python computing language and are run on the receiving computer. Incoming digital complex samples are decoded using the compressed sensing approach developed by Urco et al. (2019). Specifically, signals are decoded using a sparse model with a combination of matched filter, inverse filter, and least square fitting, and yield the signal from each transmitter on each receiver. Combinatorics indicate that in the case of a typical MISO configuration (five transmitters and one receiver with two polarizations) 10 complex signals are obtained. Fifty complex signals are obtained in the case of a MIMO configuration consisting of five transmitters and five receivers with two polarizations each. The decoded signals are incoherently combined to detect echoes, and the decoded signals are stored. The received complex signals of the two linear polarizations are coherently combined taking into account their polarization angle. This operation allows us to use all the available power on reception, since the received signals are in general elliptically polarized depending on the bistatic geometry, the orientation, and location of the echoes. After coherent combination, auto and cross correlations are estimated to determine Doppler shift, correlation time, amplitudes, and interferometric phases using fitting approaches (parameter estimation). Depending on the goodness of fit and the characteristics of the detected echoes, events are selected and identified for further processing. The parameters of identified events and geometry calculations, assuming the system is phase calibrated, for each link are recorded on site and sent via internet to a central server. Separate system phase calibration is performed. Geometry calculations take into account the Earth's curvature and produce estimates of the latitude, longitude, altitude, and Bragg wave vector (see below) for each identified event. On-site, mean winds are estimated, visualized, and stored for monitoring and quality control purposes.

2.2. Peru Deployment

The SIMONe Peru system is a specific implementation of the SIMONe concept, and currently consists of one transmitter site located at the JRO (11.95°S, 76.87°W, 540.55 m) and five receiver stations located between 30 and 180 km from JRO. The operating frequency is 32.55 MHz. The transmitter site is composed of five linearly polarized two-element Yagi antennas, with the elements aligned in the East-West direction, located at positions (x, y, z): (11.71, −15.8, 0), (18.428, 6.345, 0.436), (−0.48, 19.58, 0.15), (−18.64, 5.66, −0.67), (−11.2, −16.067, −0.732), respectively, in meters with respect to the center of the array. Note that the interferometry configuration is a pentagon and all the antennas are not on plane, that is, z is not zero for all the antennas. The use of a pentagon configuration in interferometric SMRs has been discussed by Younger and Reid (2017) and Chau and Clahsen (2019). Point-spread functions of pentagon configured multistatic SMRs

Table 1
SIMONe Peru Receiving Stations Used Between September 2019 and April 2020

Receiver	Latitude (°)	Longitude (°)	Altitude (m)	Start date	End date
Ancon	−11.77	−77.15	72.00	2019-09-02	running
Azpitia	−12.59	−76.62	69.92	2019-10-04	running
Huancayo	−12.04	−75.32	3335.20	2019-09-02	running
Sta Rosa	−11.66	−76.79	1160.75	2020-02-27	running
Barranca	−10.80	−77.73	60.64	2019-09-04	2020-02-05
Huacho	−11.12	−77.61	58.10	2019-10-04	2020-02-05
La Cantuta	−11.96	−76.70	947.67	2020-02-11	2020-02-16
Mala	−12.66	−76.63	49.66	2019-08-28	2019-10-04
Obrajillo	−11.45	−76.62	2731.92	2020-02-05	2020-02-27
Oyon	−10.67	−76.77	3677.93	2019-11-08	2020-01-06

show sidelobes with lower amplitude, more angular separation and better symmetry than those obtained with the Jones configuration that is used in most monostatic SMRs (e.g., Jones et al., 1998).

Each receiver site consists of one cross-polarized two-element Yagi antenna, where each linear polarization is received independently. A list of the receiver sites, their location, and time of operations between September 2019 and April 2020 is given in Table 1. Although our current system consists of only five receiver units, during this time period we have located them at more sites due to: (a) logistical issues (e.g., unexpected electromagnetic interference), and (b) exploration of potential sites for future campaigns with more receiving stations.

Since the transmitter site uses multiple transmitters (five) and each receiver site uses only one receiver antenna, the current version of SIMONe Peru therefore operates in a MISO configuration. Each transmitter uses a different pseudorandom code of 1,000 bauds with baud length of 10 μs, so the waveform sequence is repeated at 10 ms intervals, providing an unambiguous total range of 3,000 km.

An example of typical detections over the JRO-Azpitia bistatic link is shown in the supporting information (Figure S1). Besides the specular meteor echoes, which are the main focus of SIMONe Peru, other echoes are also noted with strong radar cross sections. In Figure S1, the strong echoes slightly above 200 km around 1800 UT are due to daytime equatorial electrojet field-aligned irregularities (e.g., Farley, 2009). Examples of other echoes are presented and discussed in Section 5.

The parameter files of each station are quality-controlled by processing at our home institute in Germany. Since the cross-correlations of all interferometric pairs are recorded for each identified event, the empirical phase calibration algorithm of Chau and Clahsen (2019) is applied where needed and a new parameter file with recalculated geometry is generated. In practice, we have only found it necessary to use empirical phase calibration during initial installation and checkout activities. Since then, the systems are hardware calibrated and exhibit long-term stability using periodic manual checks. Motivated by the detection of strong daytime EEJ echoes and concerns about their effect on core MLT processing, we implemented additional quality control measures through use of the clustering algorithm DBSCAN (Ester et al., 1996) to find clusters of echoes along individual range, time, and angle axes and remove them. The process is robust to the SMR application because specular meteor echoes are not expected to be clustered in all three variables. After the DBSCAN based quality control process, the files of all links are combined into a metastructure known as a multilink file. Figure 2 shows an example of a few days of observations in December 2019 after combining the five links. These files are stored in our database and used in the results presented below.

In Figure 3, we show a map with all SIMONe Peru stations between October 2019 and April 2020, where blue represents the transmitter station. The receiving stations are represented by: green (currently running), yellow (waiting to resume operations), red (tested but currently not in operation). The right panel shows a summary of operations during the first 6 months: (top) normalized counts color coded by links, and (bottom) average total daily count for each month. The links with the most meteor detections are JRO-Azpitia and JRO-Ancon. Seasonally, December is the month with most events (more than 40,000 per day). Note that in January, the JRO-Ancon link shows significantly fewer counts than December and February due to a site problem with electricity and internet during that month.

3. Wind Processing

The phase of the received complex voltage at receiving antenna m due to a meteor echo located in the far field and illuminated by transmitter p, that is, phase of V_{mp}, is:

$$\phi_{mp} = -(\mathbf{k}_i - \mathbf{k}_s) \cdot \mathbf{u}t - \mathbf{k}_i \cdot \mathbf{R}_p - \mathbf{k}_s \cdot \mathbf{R}_m \quad (1)$$

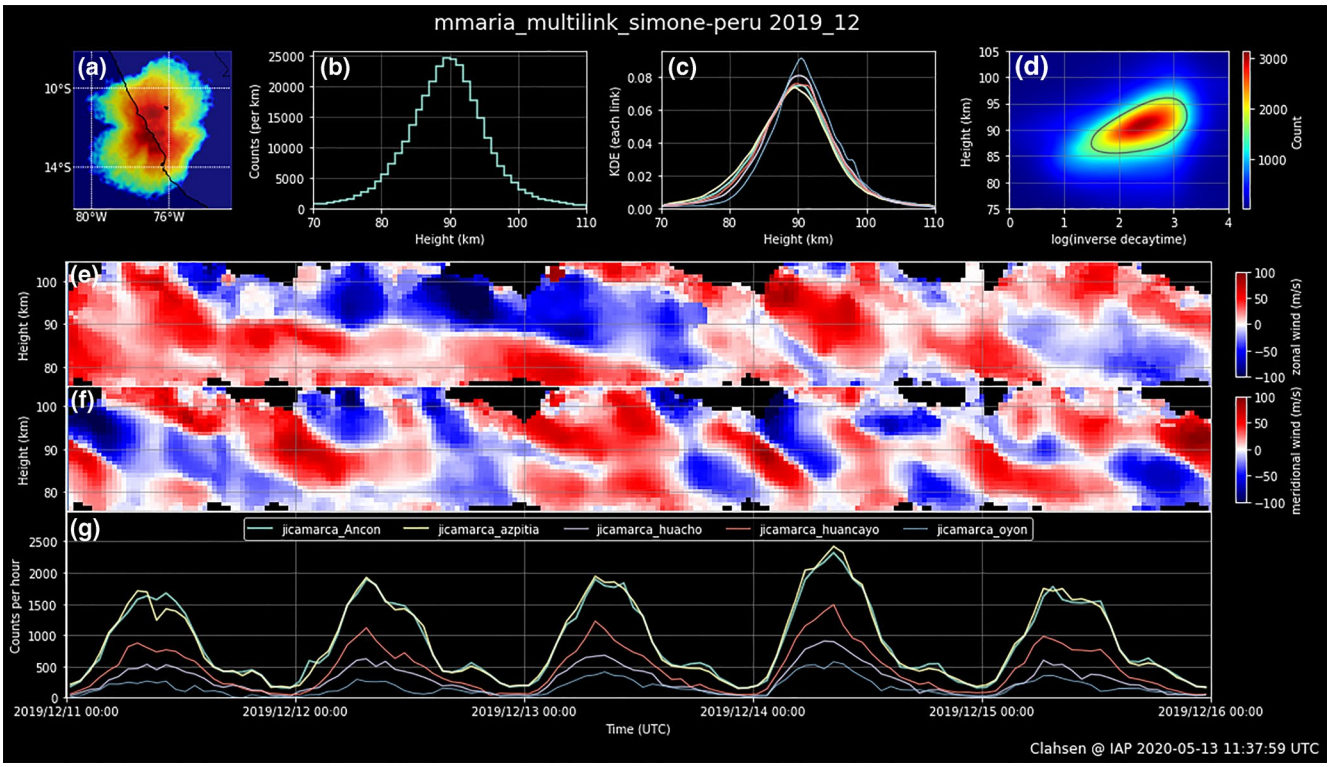

Figure 2. Example of parameters obtained after combining five SIMONe Peru links: (a) 2-D histogram of detections on latitude versus longitude axes, (b) altitude distributions across all links, (c) altitude distribution of each link, (d) 2-D histogram altitude versus inverse decay time, (e) mean zonal winds, (f) mean meridional winds, and (g) counts per hour for each bistatic link.

where $\mathbf{R}_p$ is the vector location of the meteor with respect to p, and $\mathbf{R}_m$ is the vector of receiver m with respect to the meteor; $\mathbf{k}_i = k\mathbf{R_p}/|\mathbf{R}_p|$ and $\mathbf{k}_s = k\mathbf{R_m}/|\mathbf{R}_m|$ are the incident and scattered wavevectors, $k = 2\pi/\lambda$, λ is the radar wavelength, and $\mathbf{u} = (u, v, w)$ is the wind velocity vector that advects the meteor trail.

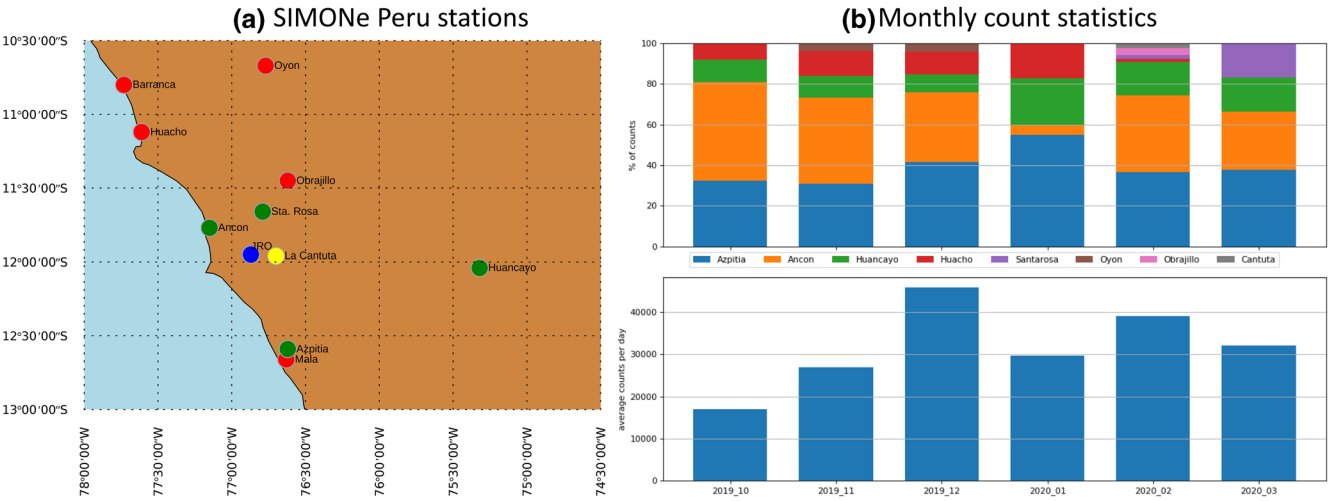

Figure 3. (a) Map showing SIMONe Peru stations: transmitter in blue and receiving stations in green, yellow and red representing running, waiting to resume operations, and tested but not running, respectively. (b) Count statistics between October 2019 and March 2020 for each month. The top graph shows the detections in percentage color coded for each link, the bottom histogram shows the average total daily counts for each month.

The zonal (u), meridional (v), and vertical (w) components of the wind are positive to the east, north, and up, respectively.

Given these definitions, the phase of the cross-correlation of voltages due to transmitters p and q of signals at receiver m evaluated at time lag τ (i.e., phase of $V_{mp}(t+\tau)V^{*}_{mq}(t)$), is given by

$$\begin{aligned}\phi_{mp,mq}(\tau) &= -(\mathbf{k}_i - \mathbf{k}_s)\cdot\mathbf{u}\tau - \mathbf{k}_i\cdot\mathbf{R}_p - \mathbf{k}_s\cdot\mathbf{R}_m + \mathbf{k}_i\cdot\mathbf{R}_q + \mathbf{k}_s\cdot\mathbf{R}_m \\ &= \mathbf{k}_B\cdot\mathbf{u}\tau + \mathbf{k}_i\cdot\Delta\mathbf{r}_{pq}\end{aligned} \tag{2}$$

where $\mathbf{k}_B = \mathbf{k}_s - \mathbf{k}_i$ is the Bragg vector, $\mathbf{R}_p - \mathbf{R}_q = -\Delta\mathbf{r}_{pq}$, $\Delta\mathbf{r}_{pq} = \mathbf{r}_p - \mathbf{r}_q$, and $\mathbf{r}_p$ and $\mathbf{r}_q$ are the vector positions of transmitting antennas p and q respect to a common reference, respectively.

Inspecting Equation 2, interferometric information $\mathbf{k}_i$ can be obtained from the cross-correlation at $\tau = 0$ for all 10 different interferometric pairs. The overall solution is obtained with a combination of beamforming and least square fitting (e.g., Chau & Clahsen, 2019, for details). The Doppler information (f_d) can be obtained from the auto-correlation at different temporal lags. The magnitude of $\mathbf{R}_i$ is obtained from the total range information, the vector difference between the receiver and transmitter positions, and $\mathbf{k}_i$ (e.g., Stober & Chau, 2015, Equation 1). Note that in MISO configurations one measures the AOD (or in our case $\mathbf{k}_i$), while in more traditional SIMO systems (single transmitter, multiple receivers), the measured quantity is the AOA (or $\mathbf{k}_s$).

Traditionally, MLT wind products from SMRs have been obtained from a straightforward binning of meteor detections in altitude (z) and time (t) with resolutions Δh and Δt, respectively. Then a mean $\mathbf{u}_0(z,t) = (u_0(z,t), v_0(z,t), w_0(z,t))$ was obtained by solving $N_m(t,z)$ sets of equations as

$$\mathbf{k}_{Bi}\cdot\mathbf{u}_0(z,t) = 2\pi f_{di} \tag{3}$$

where $\mathbf{k}_{Bi}$ and f_{di} are the Bragg vector and Doppler shift of detection i in the $N_m(t,z)$ set. The solution of this method is assumed to represent an average of the true wind field over the horizontal region sample. Equivalently, the wind field is assumed homogeneous over the sampled region. The solution under these assumption is obtained using a doubly iterated weighted least square fitting approach. In the first fitting, the Doppler uncertainties are used as weights, while in the second run detections with differences more than three times the standard deviation are not considered, and the absolute differences are used as weights. The latter is implemented to propagate uncertainties to $\mathbf{u}_0$ considering not only the uncertainties in Doppler estimation, but also geophysical variability. The estimates using Equation 3 are labeled below as M1 (method 1 or homogeneous).

The homogeneous method estimates mean winds within the radar illuminated area of ~400 km diameter, and has been employed for many decades to study large-scale dynamics of MLT winds (i.e., planetary waves and tides), either using single SMR stations (e.g., Hoffmann et al., 2007) or using multiple SMR stations to get wavenumber information (e.g., He & Chau, 2019; Manson et al., 2009). However, wind dynamics with smaller scales (time scales less than a few hours, horizontal scales less than 400 km, and vertical scales less than 4 km) are expected to be filtered out with M1.

In this study, we take advantage of additional multistatic count statistics and more importantly the multistatic geometry's inherent provision of different viewing angles to implement two other new methods yielding wind fields with horizontal information: (a) a gradient method (M2) and (b) a method that uses inverse theory (M3).

3.1. Gradient Method

In the gradient method, the wind field inside the observed volume is approximated by its first-order Taylor expansion terms, that is,

$$\begin{aligned}\mathbf{u}(x,y,z,t) &\approx \mathbf{u}_0 + \frac{d\mathbf{u}}{dx}(x-x_0)\frac{d\mathbf{u}}{dy}(y-y_0) + \frac{d\mathbf{u}}{dz}(z-z_0) \\ &\approx \mathbf{u}_0 + \mathbf{u}_x(x-x_0) + \mathbf{u}_y(y-y_0) + \mathbf{u}_z(z-z_0)\end{aligned} \tag{4}$$

where (x_0, y_0, z_0) is a reference point, (x, y, z) is the location where the velocity is evaluated, and

$$\begin{aligned}\mathbf{u}_x &= (du/dx, dv/dx, dw/dx) \\ \mathbf{u}_y &= (du/dy, dv/dy, dw/dy) \\ \mathbf{u}_z &= (du/dz, dv/dz, dw/dz)\end{aligned}$$

The positions (x, y, z) are calculated in kilometers taking into account latitude, longitude, and altitude of each detection and the Earth's radius at the reference point. The gradient approximation in spherical coordinates can be found in Appendix A of Chau et al. (2017).

Using $\mathbf{u}(x,y,z,t)$ from Equation 4 in Equation 3 instead of $\mathbf{u}_0(z,t)$, the mean values (u_0, v_0, w_0) and the gradients of the horizontal wind components $(u_x, u_y, u_z, v_x, v_y, v_z)$ are obtained from solving the set of $N_m(t, z)$ equations

$$\mathbf{k}_{Bi} \cdot \mathbf{u}(x,y,z,t) = 2\pi f_{di} \tag{5}$$

As in the case of M1, the solutions are found using a doubly iterated weighted least square fitting. However, note that in the multistatic case we fit for nine parameters instead of three, so more detections than for M1 are required. In our M2 implementation, we have used a minimum of 10 detections including at least two different links. The latter is to avoid having all detections from a single link, which do not allow the estimation of vorticity (e.g., Chau et al., 2017). In this work, we have not fitted for the gradients of w, that is, dw/dx, dw/dy, dw/dz, but this can be done in future work.

Similar gradient analysis approaches have been applied in the lower atmosphere (e.g., Browning & Wexler, 1968; Waldteufel & Corbin, 1979) and thermosphere (e.g., Conde & Smith, 1998; Meriwether et al., 2008). However, since most of these previous efforts were applied to monostatic systems, the relative vorticity (see below) was not measured directly. Instead, this parameter was usually derived assuming local time and longitude were interchangeable (e.g., Burnside et al., 1981).

Following meteorological terminology (e.g., Wallace & Hobbs, 2006, Chapter 7), the horizontal gradient terms of the horizontal components can be combined to obtain

$$\nabla_H \cdot \mathbf{u} = u_x + v_y \quad \text{Horizontal divergence} \tag{6}$$

$$\zeta = v_x - u_y \quad \text{Relative vorticity} \tag{7}$$

$$\text{Stretching deformation} = u_x - v_y \tag{8}$$

$$\text{Shearing deformation} = v_x + u_y \tag{9}$$

We have implemented expressions for horizontal divergence and relative vorticity that take into account the latitude information (see Chau et al., 2017, Equations A15 and A16, respectively). Due to the SIMONe Peru low latitude location (12°S), the results do not vary much as a function of latitude, so this information is not included.

We note that M2 improves on M1 analysis by providing spatial information of the wind field inside the observed volume. However, small structures would be smoothed out, as this information would be in the second- and higher-order terms if Taylor expansion was further extended. In addition, M2 approaches can introduce artificial structure, and is particularly true for regions with few or noisy measurements.

3.2. Regularized Wind Field Inversion Method

In order to explore smaller spatial scales that could be filtered out in M2 (see previous) and to avoid generation of artificial structures due to noisy measurements, in this work we have implemented a third approach (M3). M3 is an extension of the Harding et al. (2015) method, which was previously applied to a network of Fabry-Perot Interferometers to measure thermospheric wind fields. This technique uses inverse theory to find the smoothest field that matches the measurements to within their average uncertainties, instead of assuming an *a priori* functional form of the wind field. In this study's context, we solve a set of equations given by Equation 5 where the unknown quantities are the values of the wind on every pixel in a high resolution grid. Regularization is needed since without it the problem is vastly underdetermined and therefore unstable, as there are more unknowns than measurements.

Written in an optimization problem and following the nomenclature of Harding et al. (2015), the problem reduces to

$$\begin{aligned} &\text{minimize} && r(\overline{u}) \\ &\text{such that} && \| \Sigma^{-1/2}(A\overline{u} - \overline{d}) \|_2^2 \leq \epsilon \end{aligned} \tag{10}$$

where $\overline{u}$ is the vector of wind components at each gridded point (x_j, y_j, z_j), A is the matrix containing the corresponding components of Bragg vector (k_{Bi}), $\overline{d}$ is the vector containing the Doppler measurements (i.e., $2\pi f_{di}$), $\| \cdot \|_2^2$ is the vector 2-norm, Σ is the measurement covariance matrix, ϵ is a tuning parameter, and $r(\overline{u})$ is a scalar-valued nonnegative function that measures the roughness of the wind field. In this work, we have considered only a curvature regularization setting $r(\overline{u}) = \| C\overline{u} \|_2^2$ (e.g., Harding et al., 2015, Equations 6–8). Similar curvature operators have been used in other physically appropriate applications that estimate vector fields (e.g., Hysell et al., 2014; Nicolls et al., 2014; Stober et al., 2018). Other regularization conditions are also possible, for example, the gradient regularization used by Harding et al. (2015), but given the large quantity of data offered by meteor radar systems, we chose a conservative approach (see below).

Then the minimization problem becomes

$$\text{minimize} \ \| \Sigma^{-1/2}(A\overline{u} - \overline{d}) \|_2^2 + \lambda_0 \| C\overline{u} \|_2^2 \tag{11}$$

taking the form of a Tikhonov regularization. Solving Equation 11 analytically (Aster et al., 2013), the solution $\overline{u}^*$ is

$$\overline{u}^* = [A^T\Sigma^{-1}A + \lambda_0 C^T C]^{-1} A^T \Sigma^{-1} \overline{d} \tag{12}$$

which can be computed using sparse matrix routines (e.g., "spsolve" from the Python "scipy" linear algebra package). More details and discussion on the implementation can be found in Harding et al. (2015).

Although the original implementation of Harding et al. (2015) was implemented at a single altitude, the extension to SIMONe data is trivial, since similar to M1 and M2, the input data is already binned into different altitudes and times. To keep some smoothness in time, Equation 12 has been solved for overlapping times. In the examples presented in this work, $\overline{u}^*$ has been obtained using meteor detections in a time interval of $\Delta_t = 30$ min, but solutions are obtained on a 15 min time cadence with spatial resolutions Δ_z, Δ_x, Δ_y at 2, 20, and 20 km, respectively. In altitude, a Gaussian weighting function with $\sigma = \Delta_z/2$ around the desired altitude $\pm 3\Delta_z/2$ has been applied.

As in any Tikhonov regularization problem, there is no single formula for selection of the optimal value of λ_0. In our case, we have first estimated λ_0 empirically using a generalized cross validation (GCV) approach using a few hours of data (e.g., Fenu et al., 2016) and then selected its median value for the examples shown in this work. In the larger context of an operational system, however, not only is using a GCV approach computationally expensive, but also more importantly there is a huge variability in the λ_0 selection that results. Such variability is particularly problematic for our multistatic SMR systems, since the number of

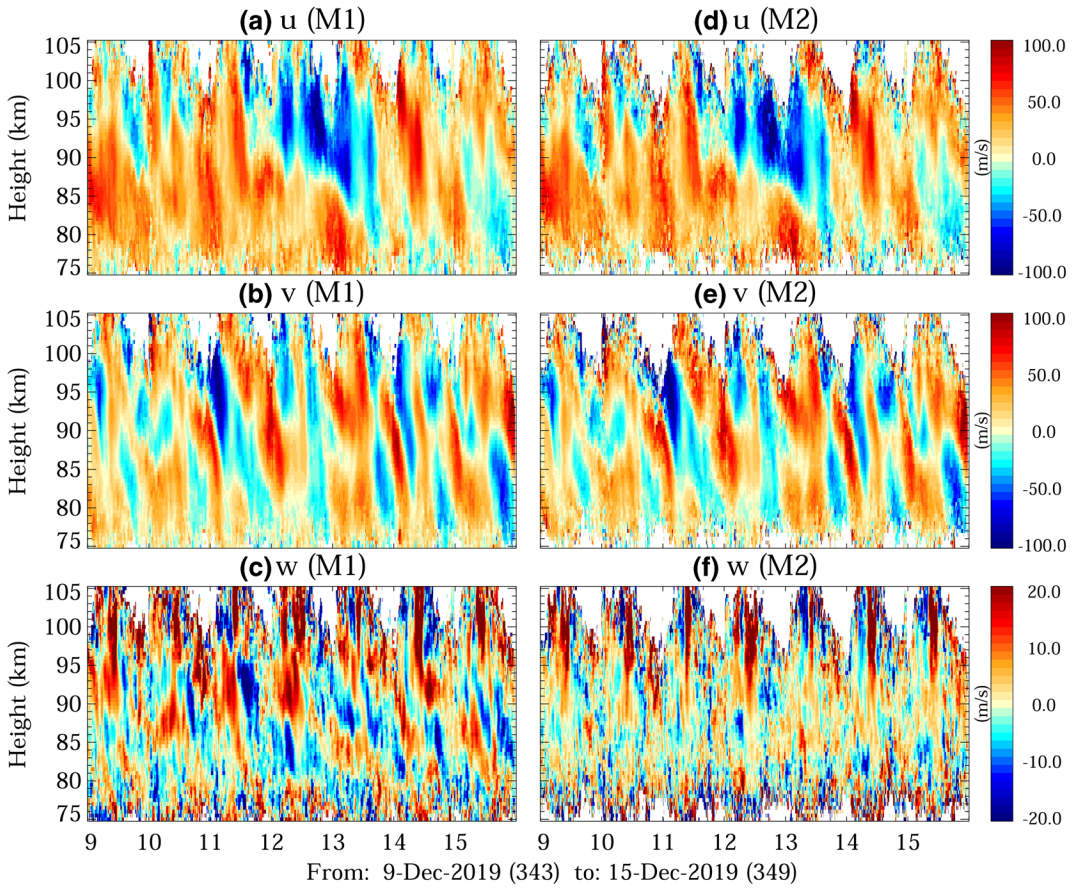

Figure 4. Mean 3-D winds between December 9 and 16, 2019 obtained with homogeneous method (M1) (left) and gradient method (M2) (right), in both cases using 1 h and 2 km bins.

counts and diversity of Bragg vectors vary widely as function of time of the day. For example, the minimum counts occur around 2300 UT every day (see Figure 2).

For this work, we have preferred to take a conservative approach and use a median value ($\lambda_0 = 1{,}000$) for all times and altitudes. This implies an intrinsic filtering (smoothing) of small scales that could be otherwise resolved using information embedded in the input data with a different regularization constraint value. Future efforts will concentrate on analysis with smaller λ_0 for appropriate selected times, as well as the extension of M3 to a fully 3D solution, instead of a 2D solution for selected altitude bins.

4. Wind Results

In this section, we present the preliminary MLT wind results obtained with SIMONe Peru using the analysis methods of Section 3). We begin with examples of derived parameters using M1 and M2, then we show results of large-scale features from M2 estimates, followed by examples of small-scale features obtained with M3.

4.1. Mean Winds and Gradients of the Horizontal Wind

In all SMRs, the main products are mean horizontal winds obtained with M1 approaches. In Figure 4, we present 7 days of mean winds obtained with M1 and M2 between December 9 and 16, 2019. The left/right column shows the zonal, meridional, and vertical components of M1/M2. Both estimates have been

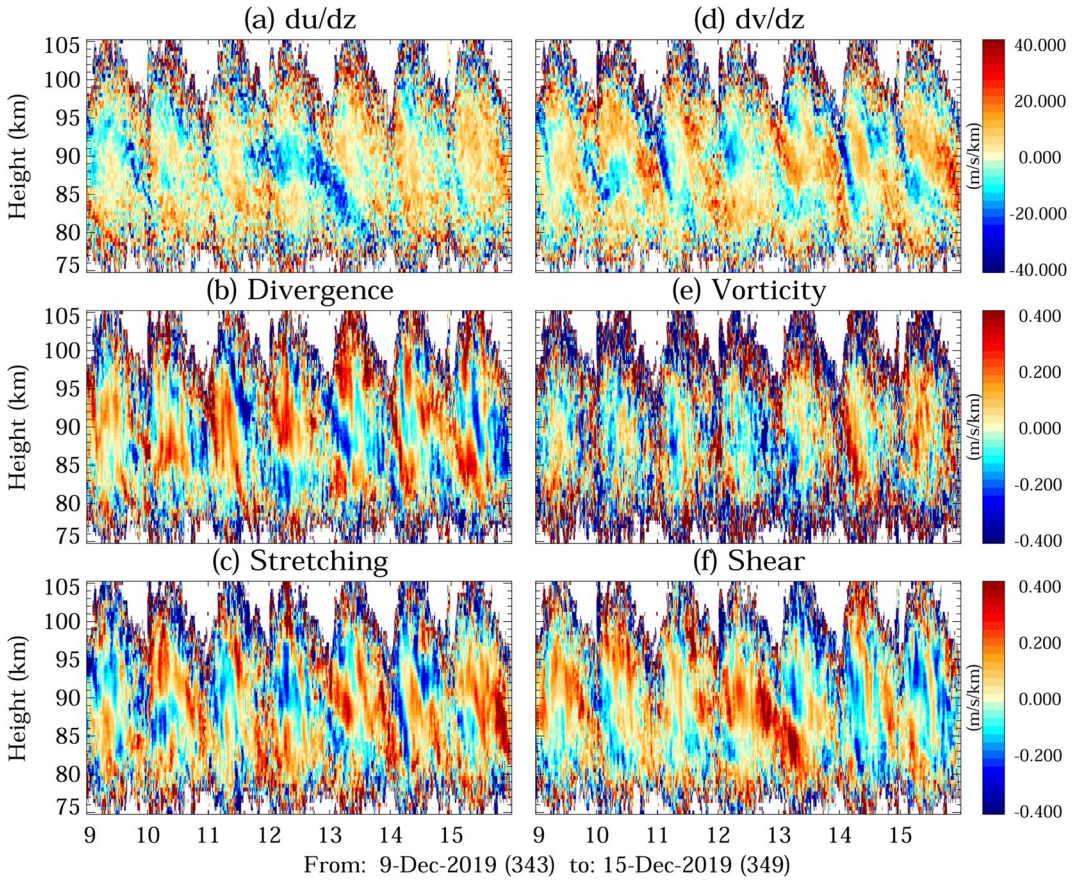

Figure 5. Derived components of horizontal winds with the gradient method (M2): (a) zonal wind vertical gradient, (b) horizontal divergence, (c) stretching deformation, (d) meridional wind vertical gradient, (e) relative vorticity (ζ), and (f) shear deformation, using the same period and sampling as in Figure 4.

obtained with 1-hour and 2-km bins, and 5-minute and 500-m sampling. From a simple visual inspection (and also from a point-to-point correlation not shown here), the zonal and meridional mean estimates with M1 and M2 are in excellent agreement. Both components show a typically expected dominant diurnal behavior with variability over time scales of a few days.

On the other hand, the mean vertical wind components produced by M1 and M2 are not in good agreement. However, both show relative large variability of a few meters per second.

Before discussing the discrepancies in vertical components, we show the gradient information of the horizontal components in Figure 5 using the same data, resolution, and sampling used in Figure 4, that is, (a) u_z, (b) Horizontal divergence ($\nabla_H \cdot \mathbf{u}$), (c) Stretching deformation, (d) v_z, (e) relative vorticity (ζ), and (f) shear deformation. In all six parameters the units are $ms^{-1}\ km^{-1}$.

All six parameters show large temporal and altitude variability with a dominant diurnal behavior. Features include (a) a large negative vertical gradient in the zonal component (u_z), accompanied by large positive shear deformation around December 13, and (b) a 24-h period large oscillation in the horizontal divergence around December 12. The variability and magnitudes of these parameters, in particular estimates of horizontal gradients, are much larger and clearer than those reported over northern Norway (69°*N*) (e.g., Chau et al., 2017, Figure 4). A direct comparison is not relevant, since the latitudes and seasons are different, but we note that it is striking to see such variability over the equatorial Peru region.

Again from a visual inspection, we qualitatively find following Chau et al. (2017) that structures in the horizontal divergence (Figure 5b) resemble the structures in M1 vertical component (Figure 4c). This indicates

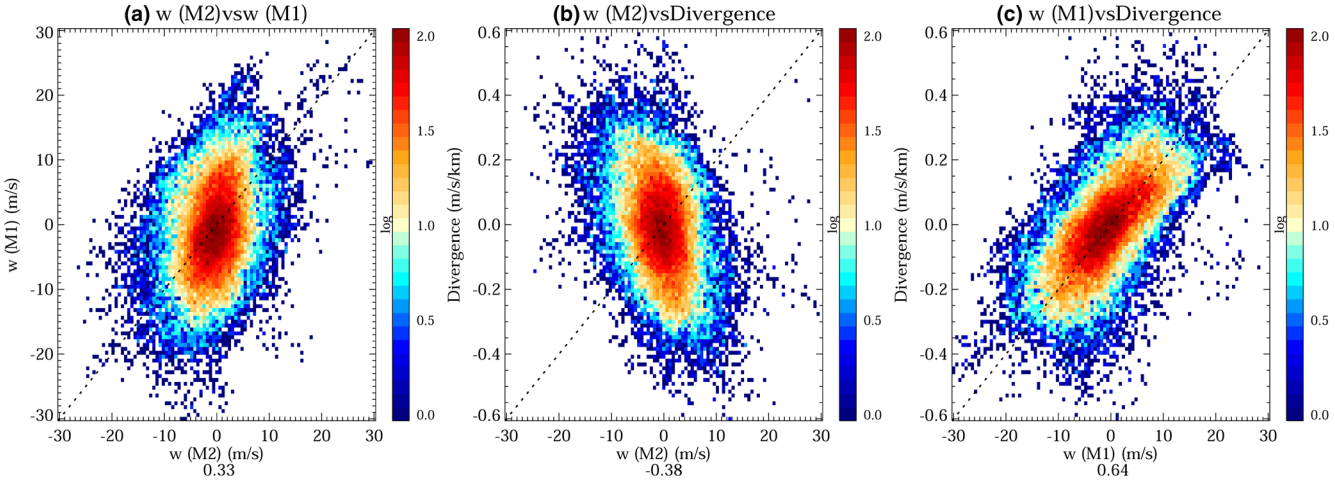

Figure 6. 2D histograms of vertical velocity estimates and horizontal divergence using the results between 82 and 92 km shown in Figures 4 and 5: (a) vertical estimates using M1 and M2, (b) vertical estimates using M2 (Figure 4f) and horizontal divergence (Figure 5b), and (c) vertical estimates using M1 (Figure 4c) and horizontal divergence. The Pearson correlation coefficient is indicated for each plot.

that vertical velocities obtained with M1, at least over relative larger areas, are significantly contaminated by horizontal divergence as also found by Chau et al. (2017).

To get a more quantitative idea of vertical component correlations, in Figure 6 we show three 2-D histograms using results between 82 and 92 km from Figures 4 and 5. Specifically, these show: (a) w (M1) versus w (M2), (b) Horizontal divergence versus w (M2), and (c) Horizontal divergence versus w (M1). The highest significant correlation is found, as expected, between the horizontal divergence and w (M1), with a Pearson correlation coefficient of 0.64. If instead estimates obtained with 4-h and 4-km bins are used, the correlation coefficient is 0.78 (results not shown here). This indicates that the observed correlation between horizontal divergence and w is mainly due to structures with medium spatial (a few hundreds of kilometers in the horizontal and more than 4 km in the vertical) and temporal (more than 4 h) scales.

We have also estimated M2 parameters using 4-h and 4-km time-altitude bins. The results are included in the supporting information in Figures S2 and S3, for the mean winds and gradients, respectively. These estimates represent detailed observations of the dynamics of large-scale processes.

4.2. Large-Scale Temporal Features

In this section, we present an overview of large-scale wind features that have been obtained with SIMONe Peru between October 2019 and March 2020. Note that although the results are not unique to multistatic configurations, our results confirm that mean horizontal wind components, in this case obtained with M2, are also useful for studies of large-scale features.

Figure 7 shows 4-day averaged zonal and meridional winds and the total amplitudes of waves with selected key periods of 48, 24, 12, 12.42, and 8 h, corresponding to the quasi-two-day, diurnal, semidiurnal, quasilunar, and terdiurnal components, respectively. All of them have been obtained using a 21-day running window and a least-square fitting approach similar to the one used by Sandford et al. (2006). The selection of a 21-day window has been done to separate the quasilunar (12.42 h) and the semidiurnal (12 h) components. Both of these components were previously observed to have large amplitudes in the northern hemisphere MLT altitudes at both mid and high latitudes, particularly between January and February months (e.g., Chau et al., 2015; He & Chau, 2019).

The salient features in Figure 7 are as follows: (a) strong planetary wave activity (with periods of a few days) in the mean zonal and meridional winds, (b) quasi-two-day and diurnal components present the largest amplitudes, (c) quasilunar and terdiurnal components present the smallest amplitudes. In the case of

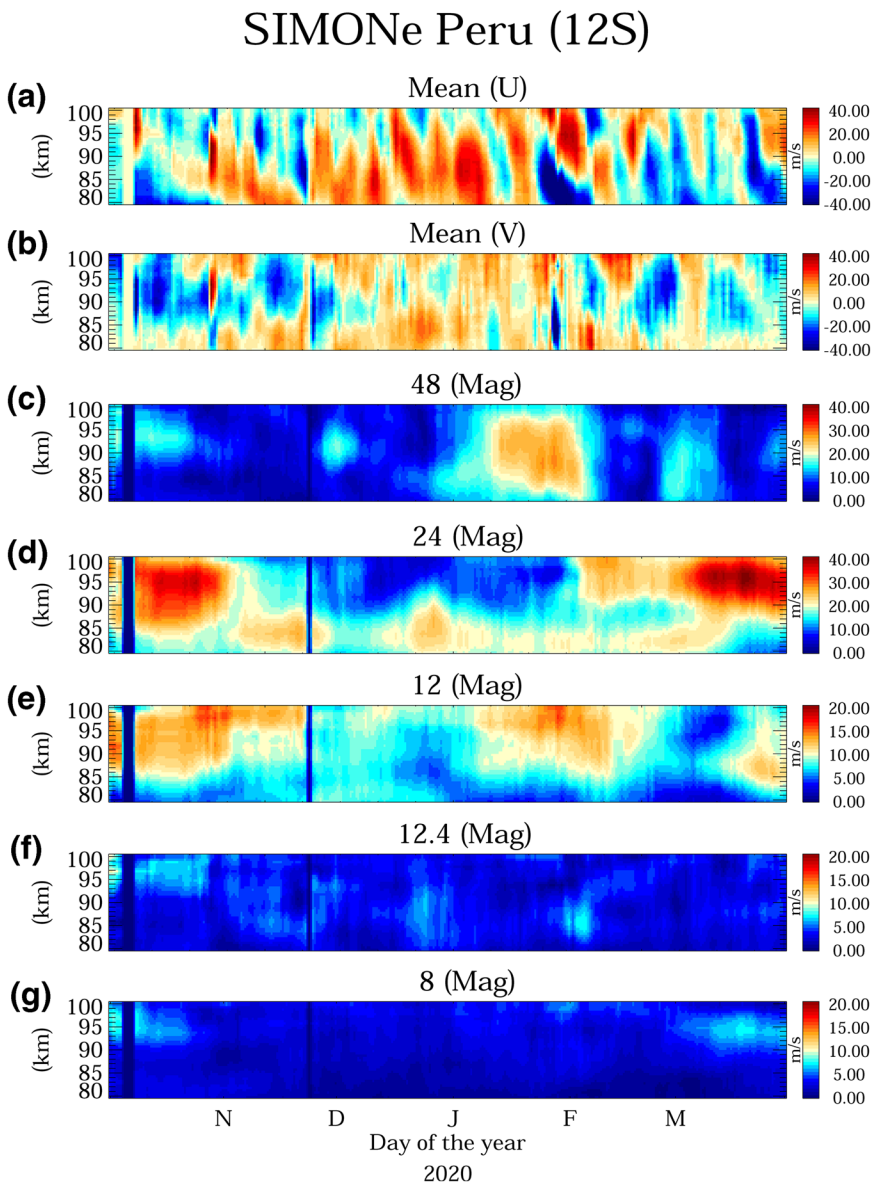

Figure 7. Mean horizontal winds and selected waves components between October 2019 and March 2020: (a) mean zonal wind, (b) mean meridional wind, (c) quasi-two-day wave, (d) total diurnal tide, (e) total semidiurnal tide, (f) quasilunar tide, and (g) total 8 h components. In the case of the wave components, the total magnitude is shown, that is, $\sqrt{u_T^2 + v_T^2}$. The mean zonal and meridional winds have been obtained with a 4-day running window, while the wave components used a 21-day running window (see text for details). Data gaps are shown with vertical yellow and dark blue narrow rectangles. Data gaps are shown with vertical yellow and dark blue narrow rectangles.

quasi-two-day and diurnal components, the largest amplitudes are observed in the meridional component. These results are in good agreement with previous low-latitude MLT studies (e.g., Araújo et al., 2014; Davis et al., 2013; Rajaram & Gurubaran, 1998).

4.3. Small-Scales

Figure 5 already shows the benefits of SIMONe Peru's multistatic approach and analysis by providing horizontal information within the observed area, in the form of horizontal divergence, relative vorticity,

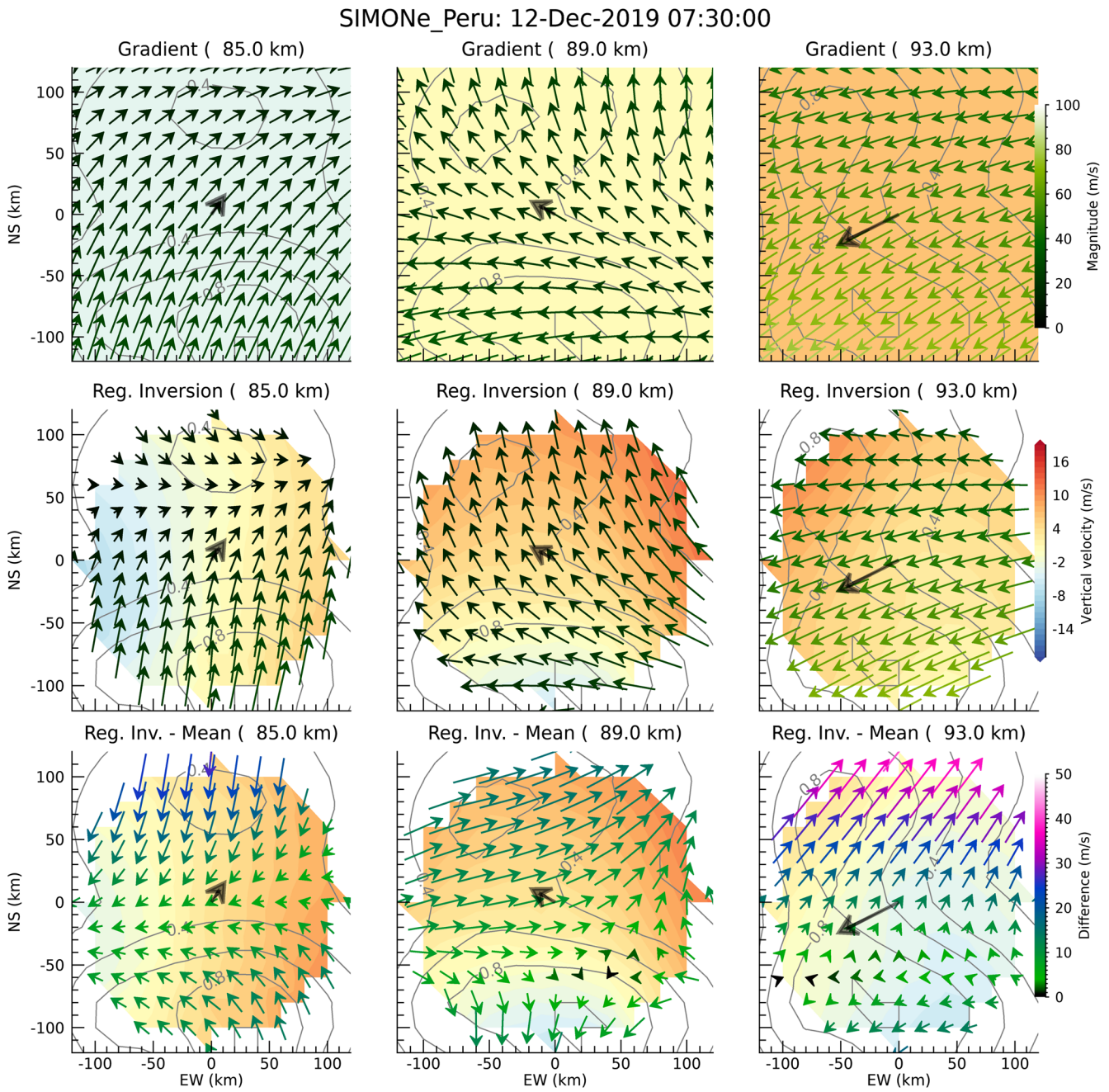

Figure 8. Wind estimates for selected heights on December 12, 2019 at 0730: (first column) 85 km, (second column) 89 km, and (third column) 93 km. The first row shows the horizontal wind field obtained with the gradient method (M2) using four-hour and four-kilometer bins; the second row shows the horizontal wind field obtained with a regularized inversion (M3); and the third row shows the wind field difference between the values in the second row and the mean horizontal wind (M2) indicated in all panels with a black arrow. In all cases the normalized meteor counts are indicated as gray contour lines, while the color contour represents the vertical component from M2 (first row), M3 (second row), and M3–M2 (third row). The color bars for the arrows representing vector fields are located to the right of each row (see text for more details).

deformation (stretching and shearing). In this section, we further extend and improve this horizontal information by implementing M3 from Section 3.2 as the regularized inversion of Harding et al. (2015).

Figure 8 shows M3 resultant mean wind fields at three selected altitudes: 85, 89, and 93 km. The first row shows the wind fields obtained with the gradient-based M2 method, but using 4-h and 4-km time-altitude bins, to preserve representation of medium and large-scale features in structures with periods larger than

4 h. The direction and magnitude are indicated with arrows. The arrows are color coded in green tones to help its visualization (upper right color bar). The contour gray lines indicate the normalized meteor counts used in the inversion while the colored background indicate the mean vertical velocity w(M2) (middle color bar). The large black arrow corresponds to the mean horizontal wind using M2, that is, (u_0, v_0), where 50 km represents 50 m/s. This mean vector and the contour gray lines are repeated in the lower two rows.

The second row shows the wind fields obtained with M3 (regularized inversion), color coded as in the first row (upper color bar). This time the colored contours show w obtained with M3 (middle colorbar). The M3 estimates have been obtained with resolutions of $\Delta z = 2$ km, $\Delta x = \Delta y = 20$ km, and $\Delta t = 30$ min. To avoid showing data with small counts and relative large zenith angles, only estimates with at least two detections and within 120 km horizontal radius over the transmitter station, are shown. Note that most estimates at large zenith angles suffer from precision issues and from poor Bragg vector diversity. The precision issue is a well-known feature of SMR with interferometry, where the zenith angle precision decreases with zenith angle, and therefore there is a large uncertainty on altitude as cited by previous studies (Hocking, 2018; Holdsworth, 2005; Vaudrin et al., 2018). The poor vector diversity issue reduces to an equivalent observation of those regions with a monostatic system.

In general, results show a reasonable agreement between M2 and M3 horizontal components. Differences are expected due to different averaging and to different conceptual implementation. In particular, in M2 we use a functional form that smooths small features, while in M3 the inversion algorithm implements smoothness regularization. In the former, one can control the amount of regularization by adjusting λ_0. As a reminder, these results have been obtained with a conservative regularization value, independent of the underlying data's number of counts or Bragg vector diversity (see above).

In the third row, we show the M3 estimates but with the mean values from M2 subtracted, through subtracting the (u_0, v_0, w_0) M2 value. Recall that these mean values are obtained with a 4-h and 4-km bin, which allows subtraction of large-scale features. In this plot row, the vectors of the horizontal wind are color-coded with the lower left color bar. The visualization attempts to remove large-scale features such as tides or waves with periods greater than 4 h that are contained in M2 estimates, yielding a representation of smaller scales. From examining the vertical velocity color contours, spatial structures of 100 km or so are evident. In the case of the horizontal wind vector, results show a mix of different flow configurations at the three altitudes: shear flow with curvatures, small vortices, convergent flows, and related structures.

Although we are confident of the general good performance of our regularized inversion approach, we emphasize that the approach taken here remains conservative and does not in particular assert that the M3 approach is necessarily superior in all situations.

For further information on results obtained with the M3 approach, the supporting information includes a movie of wind field frames obtained every 15 min between December 11 and 13, 2019. We have selected this time period due to: (a) good coverage with all five receiving stations (Figure 2), (b) diurnal tide amplitude that is smaller at the upper altitudes (Figure 7), and (c) large localized variability in derived parameters from horizontal gradients of the horizontal wind components (Figure 5). In general, the observed features in the third row supplemental plots appear to be of geophysical nature in all three components. However, clear examples of questionable results are observed around 2300 UT, when the meteor count statistics are relatively smaller (Figure 2).

5. Nonwind Results

Although the focus of this study is primarily on MLT winds, we briefly show in this section that SIMONe Peru is also able to detect other echoes with relatively large radar cross sections. One of the obvious application targets are airplanes (not shown here) that in pulsed systems could be range aliased due to radar ambiguity issues. In our case, the coded-CW implementation inherently provides very clean range-Doppler ambiguity characteristics, and our effective maximum unambiguous total range in our standard analysis is 6,000 km.

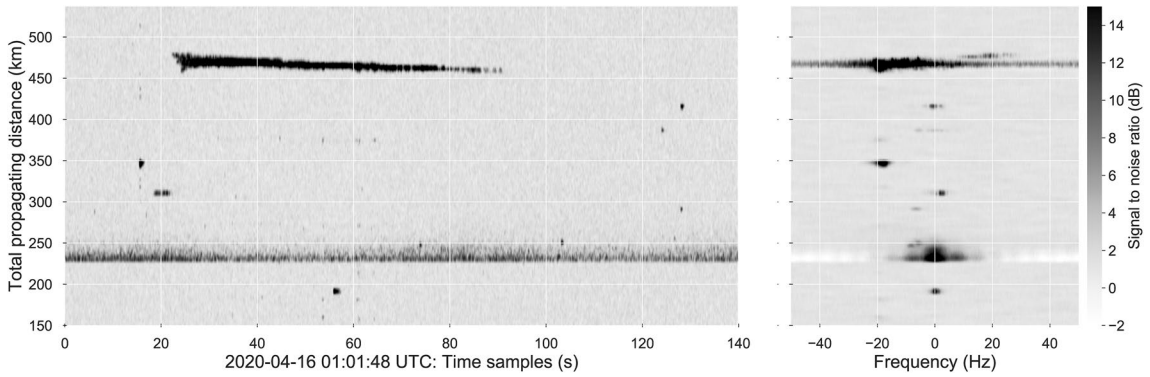

Figure 9. Range time intensity (RTI) (left) and spectrogram (right) for a selected period of 140 s on April 16 01:01:48 UT obtained with the JRO-Azpitia link. Besides the sporadic specular meteor echoes, nonspecular meteor echoes are observed above 450 km lasting more than a minute and nighttime EEJ echoes are observed around 230–250 km.

Other low-latitude geophysical echoes with strong cross-sections that are routinely observed with SIMONe Peru include: (a) daytime EEJ echoes (e.g., Farley, 2009), (b) nighttime EEJ echoes (e.g., Hysell & Chau, 2002), (c) nonspecular meteor echoes (Chapin & Kudeki, 1994), and (d) strong meteor-head echoes (e.g., Chau & Woodman, 2004). Figure 9 shows a range-time intensity (RTI) and spectrogram of decoded signals (incoherently integrated among interferometric channels) taken on April 16 at 01:01:48 UT with the JRO-Azpitia link. Besides some specular meteor echoes employed for MLT wind observations, we observed: (a) nighttime EEJ echoes around 240 km, accompanied by a narrow spectra centered at zero frequency, (b) a long-lasting nonspecular meteor trail around 460 km lasting for more than 1 minute, with different Doppler shifts depending on total range (negative at closer range, positive at further ranges), and (c) shorter-lived nonspecular echoes at different ranges and times.

Strong nonspecular echoes observed at relatively small zenith angles (<20°) can also be employed to derive MLT wind profiles (e.g., Oppenheim et al., 2009). Similarly, wide beam observations of daytime and night EEJ echoes can be routinely obtained over the middle point of each link. The current SIMONe Peru configuration would allow these observations simultaneously over five different locations, enabling studies of spatial EEJ diversity.

The nonspecular echoes, particularly those with strong and long-lasting features, can be also used to determine the atmospheric entry location of the bolide that generates the echoes, and perhaps even its trajectory when they are observed with multiple views at relative small zenith angles (<20°). Figure 10 shows a zoomed version of the long-lasting event showed in Figure 9 with JRO-Azpitia, but also the RTIs with JRO-Huancayo and JRO-Santa Rosa. Note that echoes are weaker in the JRO-Santa Rosa link not for geophysical reasons but due to a failure in the front-ends (AFEs) of one of the linearly polarized receiving channel. Using the total range information provided by these three links, we were able to estimate the entry point of the bolide that created the echoes as 14.1808°S, 76.8774°W, 96,654 m. These location is in excellent agreement with visual observations.

These events have been obtained directly from the raw data files using only the reading and decoding blocks, and therefore have not been processed with our routine RSP. Once the signals are decoded, the rest of the analysis is similar to pulse-pulse analysis used in many coherent radars, like the so-called Mesosphere-Stratosphere-Troposphere (MST) radars (Woodman & Guillén, 1974). In principle, one would need to add new detection and estimation boxes to work in parallel to our routine RSP, but this is straightforward due to the SIMONe architecture.

Probing further yields several interesting features of this bolide event. We used a special range-Doppler matched filter analysis to treat the length of each baud as the effective IPP (i.e., 10 μs). Through subsequent use of matched filter decoding (1,000 bauds), we were then also able to detect the meteor-head echo created by the ablating plasma in front of the bolide as having radial velocity close 6 km/s (1.2 kHz/s spectral motion). The output of the range-Doppler matched filter bank analysis, providing echo power as a function of

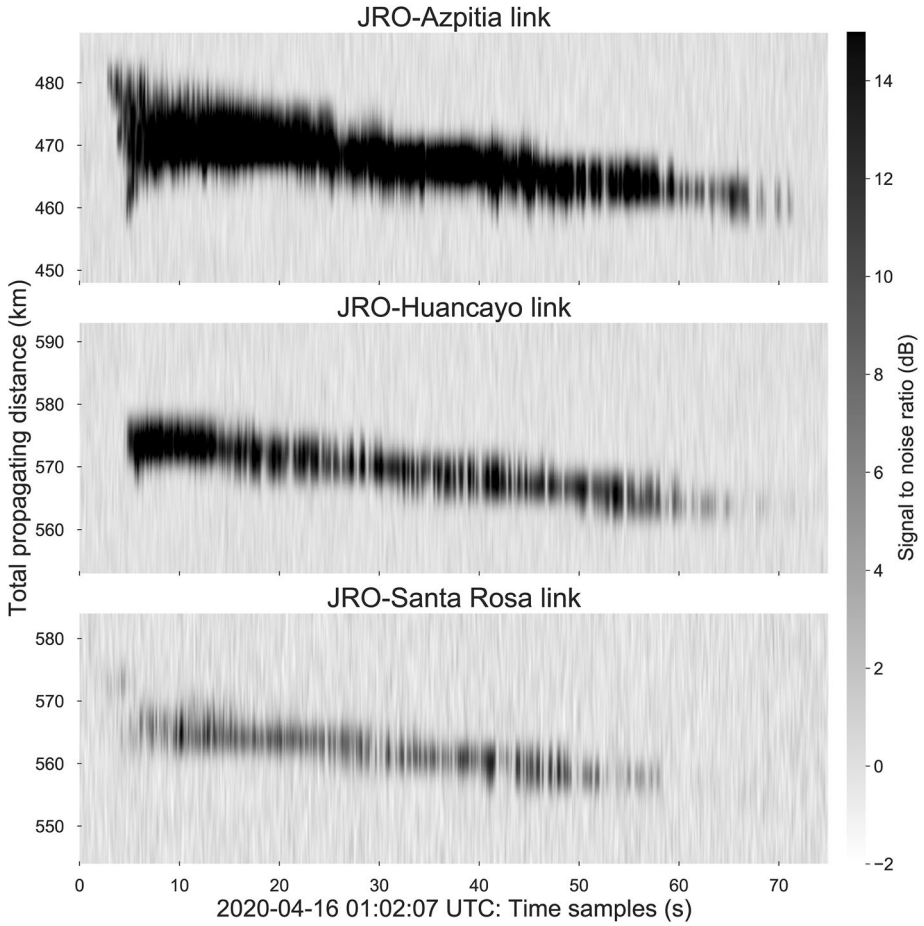

Figure 10. RTI of the strong nonspecular echo shown in Figure 9, but over three bistatic links: JRO-Azpitia, JRO-Huancayo, and JRO-Santa Rosa.

time and range is shown in Figure 11. In this figure, the head echo corresponding to the plasma surrounding the ablating meteoroid is visible moving from 470 to 460 km distance near 01:02:11 UTC, followed by the longer lived trail echoes formed after the pass of the meteoroid shown in Figure 10. Figure 12 shows further analysis from this data producing estimated range and range-rate for the head echo. This analysis, although computationally intensive, is useful to avoid range and frequency ambiguities. This approach has a maximum unambiguous range which remains at 6,000 km, with range-aliasing converted into an increase of flat noise by the pseudorandom nature of the code, and an unaliased Doppler extent of ±230 km/s (Nyquist frequency = 50 kHz). We note that a very similar approach has been applied successfully to E-region plasma irregularity studies using the radar aurora system called ICEBEAR (e.g., Huyghebaert et al., 2019).

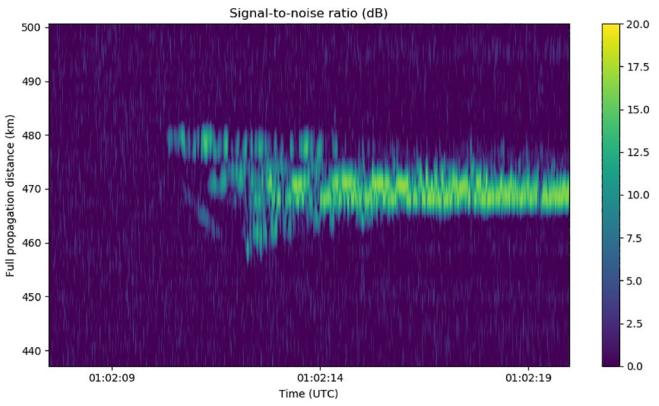

Figure 11. Range-Doppler matched filter bank output for the Peru bolide.

6. Concluding Remarks

We have shown in this paper that SIMONe Peru has been successfully implemented for studies of MLT dynamics at low latitudes at different scales. The typical large-scale features studied with monostatic SMRs are clearly observed with the system. However, since the horizontal scales of these features are much larger than the observed area, new and exciting contributions at these scales can be provided by future coordinated

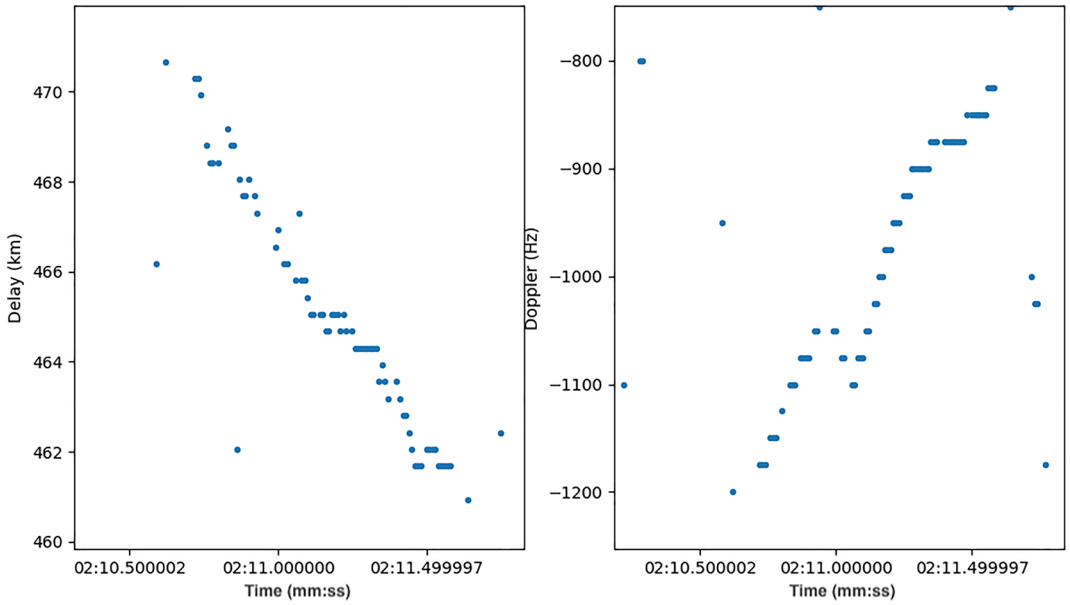

Figure 12. Range and Doppler shift estimated for the bolide head echo. Note that the times are indicated in minutes (mm) and seconds (ss), that is, mm:ss with respect to April 16, 2020, 01 h.

observations that complement SIMONe Peru measurements with other existing ground-based radars (like those from Brazil, India, Indonesia) (Araújo et al., 2014; Rajaram & Gurubaran, 1998; Rao et al., 2014). These coordinated observations have considerable potential for separation of the space-time features of tides and planetary waves, similar to He and Chau (2019).

In the case of medium scales, one of the direct contributions of multistatic systems such as SIMONe Peru lies in improved estimation of the vertical velocity when using relative large areas, by estimating the horizontal gradients of the horizontal wind, that is, w (M2). If the number of detections is sufficient in a narrow region, that is, at least 10, vertical velocities with less horizontal divergence contamination can be estimated. This narrow region approach has been implemented to study the vertical velocities of planetary waves at times of maximum meteor counts occurring only a few hours per day (e.g., Babu et al., 2012; Egito et al., 2016). We have implemented such approach using an area with 40 km radius, and indeed the resulting w (M1) and w (M2) estimates are in excellent agreement (results not shown here). Future work will provide focused study of vertical velocities obtained with M2 and M3 and their observed large variability and relative large amplitudes, leading to implications for the dynamics and electrodynamics of the equatorial MLT and the E-region dynamo regions.

With the gradient method (M2), we are now able to characterize wind fields over the observed area with nine parameters instead of the traditional three parameters (u_0, v_0, w_0). A simple extension of this method could be done by including higher-order terms or even cross terms. However, we have preferred to use a method at present that uses inverse theory and Tikhonov regularization. As in any inverse theory problem, there are different ways to approach the under determined problem. In this study, we have extended the method of Harding et al. (2015) with encouraging results despite the conservative approach we have taken (use of a single λ_0 for all cases). However, we plan to extend this method further in the future to consider a true 3-D solution (and not 2-D solutions for different altitude cuts). This will include an adaptive selection of the regularizing factor λ_0 that takes into account the data sampling and Bragg vector diversity variables. On top of these improvements, we expect that M3 would definitely outperform M2 as more links, including MIMO links, are added, since this allows not only more count statistics but also more Bragg vector diversity. The resulting structure information scales naturally with the information provided in the data.

Although not included in this work, the SIMONe Peru data can also address smaller scales in neutral motions on a statistical basis, by using the second-order statistics of line-of-sight velocities. For example,

average momentum fluxes can be obtained using zero-lag second-order statistics (e.g., Hocking, 2005). The method has been applied with varying degrees of success using monostatic SMRs. Slight improvements have been obtained using a bistatic approach by Spargo et al. (2019). Recently, Vierinen et al. (2019) has extended the concept to use nonzero spatial and temporal lags. This allows the exciting and information-rich possibility of statistical estimation of correlation, structure, and spectral functions of kinetic energy and momentum flux at different spatial and temporal scales.

Furthermore, SIMONe data from specular echoes could also be used to measure temperature, neutral density and meteor orbits as has been done with monostatic systems (e.g., Hocking et al., 2001; Holdsworth et al., 2004; Tsutsumi et al., 1999). In addition with some software improvements, SIMONe data can also be used to routinely observe strong coherent VHF radar echoes as presented by the example here. In particular, for the case of SIMONe Peru, we have shown examples of day and nighttime EEJ, nonspecular meteor and meteor-head echoes. The latter echoes could be used to detect bolides as our initial analysis demonstrated.

Finally, SIMONe Peru is centered at the multifaceted JRO complex, where multiple-technique and multi-instrument campaigns could be implemented in the future for cross-validation purposes and, more importantly, to study processes that are difficult to address with a single instrument or technique. One of such future campaigns could target the simultaneous use of JRO's different observational modes: MST (60–85 km winds) (Lee et al., 2019), oblique daytime EEJ (95–110 km zonal winds) (Shume et al., 2005), nonspecular meteor echoes (90–110 km horizontal winds) (Oppenheim et al., 2009), and optical remote sensing instruments, e.g., Near Infrared Airglow Camera on the International Space Station or the Michelson Interferometer for Global High-resolution Thermospheric Imaging on the ICON NASA explorer (e.g., Harding et al., 2017).

Data Availability Statement

Data used to generate the plots presented in this work can be found in HDF5 at https://dx.doi.org/10.22000/355

Acknowledgments
The authors thank Carsten Schult for calculating the location of the bolide, and the Jicamarca Radio Observatory (JRO) staff that supported the installation and continue supporting the maintenance and operations of SIMONe Peru. J. L. Chau appreciates useful comments from Sixto Gonzalez on early drafts. JRO is a facility of the Instituto Geofisico del Peru operated with support from the NSF AGS-1433968 through Cornell University. SIMONe analysis efforts derived from partial support from US National Science Foundation grant AGS-1626041 to the Massachusetts Institute of Technology. This work was partially supported by the Deutsche Forschungsgemeinschaft (DFG, German Research Foundation) under SPP 1788 (DynamicEarth)-CH1482/2-1 and under SPP 1788 (CoSIP)-CH1482/3-1.

References

Abdu, M. A., Brum, C. G., Batista, P. P., Gurubaran, S., Pancheva, D., Bageston, J. V., & Takahashi, H. (2015). Fast and Ultrafast Kelvin wave modulations of the equatorial evening f region vertical drift and spread f development Aeronomy. *Earth, Planets and Space*, *67*(1), 1. https://doi.org/10.1186/s40623-014-0143-5

Andrioli, V. F., Fritts, D. C., Batista, P. P., & Clemesha, B. R. (2013). Improved analysis of all-sky meteor radar measurements of gravity wave variances and momentum fluxes. *Annales Geophysicae*, *31*(5), 889–908. https://doi.org/10.5194/angeo-31-889-2013

Araújo, L. R., Lima, L. M., Batista, P. P., Clemesha, B. R., & Takahashi, H. (2014). Planetary wave seasonality from meteor wind measurements at 7.4° S and 22.7° S. *Annales Geophysicae*, *32*(5), 519–531. https://doi.org/10.5194/angeo-32-519-2014

Aster, R. C., Borchers, B., & Thurber, C. H. (2013). *Parameter estimation and inverse problems* (2nd ed.). Elsevier. https://doi.org/10.1016/C2009-0-61134-X. Retrieved from https://www.sciencedirect.com/book/9780123850485/parameter-estimation-and-inverse-problems.

Babu, V. S., Ramkumar, G., & John, S. R. (2012). Seasonal variation of planetary wave momentum flux and the forcing towards mean flow acceleration in the MLT region. *Journal of Atmospheric and Solar-Terrestrial Physics*, *78–79*(C), 53–61. https://doi.org/10.1016/j.jastp.2011.05.010

Browning, K. A., & Wexler, R. (1968). The determination of kinematic properties of a wind field using Doppler radar. *Journal of Applied Meteorology*, *7*(1), 105–113. https://doi.org/10.1175/1520-0450(1968)007{\$}{{\$}0105:TDOKPO{\$}}{\$}2.0.CO;2

Burnside, R. G., Herrero, F. A., Meriwether, J. W., & Walker, J. C. G. (1981). Optical observations of thermospheric dynamics at Arecibo. *Journal of Geophysical Research*, *86*, 5532–5540.

Chapin, E., & Kudeki, E. (1994). Radar interferometric imaging studies of long-duration meteor echoes observed at Jicamarca. *Journal of Geophysical Research*, *99*, 8937–8949.

Chau, J. L., & Clahsen, M. (2019). Empirical phase calibration for multi-static specular meteor radars using a beam-forming approach. *Radio Science*, *54*(1), 60–71. https://doi.org/10.1029/2018RS006741

Chau, J. L., Fejer, B. G., & Goncharenko, L. P. (2009). Quiet variability of equatorial **E**×**B** drifts during a sudden stratospheric warming event. *Geophysical Research Letters*, *36*(5), 1–4. https://doi.org/10.1029/2008GL036785

Chau, J. L., Goncharenko, L. P., Fejer, B. G., & Liu, H. L. (2012). Equatorial and low latitude ionospheric effects during sudden stratospheric warming events. *Space Science Reviews*, *168*, 385.

Chau, J. L., Hoffmann, P., Pedatella, N. M., Matthias, V., & Stober, G. (2015). Upper mesospheric lunar tides over middle and high latitudes during sudden stratospheric warming events. *Journal of Geophysical Research: Space Physics*, *120*(4), 3084–3096. https://doi.org/10.1002/2015JA020998

Chau, J. L., Stober, G., Hall, C. M., Tsutsumi, M., Laskar, F. I., & Hoffmann, P. (2017). Polar mesospheric horizontal divergence and relative vorticity measurements using multiple specular meteor radars. *Radio Science*, *52*(7), 811–828. https://doi.org/10.1002/2016RS006225

Chau, J. L., Urco, J. M., Vierinen, J. P., Volz, R. A., Clahsen, M., Pfeffer, N., & Trautner, J. (2019). Novel specular meteor radar systems using coherent MIMO techniques to study the mesosphere and lower thermosphere. *Atmospheric Measurement Techniques*, *12*, 2113–2127. https://doi.org/10.5194/amt-12-2113-2019

Chau, J. L., & Woodman, R. F. (2004). Observations of meteor-head echoes using the Jicamarca 50 MHz radar in interferometer mode. *Atmospheric Chemistry and Physics*, *4*, 511–521.

Conde, M., & Smith, R. W. (1998). Spatial structure in the thermospheric horizontal wind above Poker Flat, Alaska, during solar minimum. *Journal of Geophysical Research*, *103*, 9449–9472. https://doi.org/10.1029/97JA03331

Davis, R. N., Du, J., Smith, A. K., Ward, W. E., & Mitchell, N. J. (2013). The diurnal and semidiurnal tides over Ascension Island (8° S, 14° W) and their interaction with the stratospheric quasi-biennial oscillation: Studies with meteor radar, eCMAM and WACCM. *Atmospheric Chemistry and Physics*, *13*, 9543–9564. https://doi.org/10.5194/acp-13-9543-2013

Egito, F., Andrioli, V. F., & Batista, P. P. (2016). Vertical winds and momentum fluxes due to equatorial planetary scale waves using all-sky meteor radar over Brazilian region. *Journal of Atmospheric and Solar-Terrestrial Physics*, *149*, 108–119. https://doi.org/10.1016/j.jastp.2016.10.005

England, S. L. (2012). A review of the effects of non-migrating atmospheric tides on the Earth's low-latitude ionosphere. *Space Science Reviews*, *168*, 211–236.

Ester, M., Kriegel, H.-P., Sander, J., & Xu, X. (1996). A density-based algorithm for discovering clusters in large spatial databases with noise. In *Kdd'96: Proceedings of the Second International Conference on Knowledge Discovery and Data Mining* (pp. 226–231). Retrieved from www.aaai.org

Farley, D. T. (2009). The equatorial E-region and its plasma instabilities: A tutorial. *Annales Geophysicae*, *27*, 1509–1520.

Fejer, B. G., Olson, M. E., Chau, J. L., Stolle, C., Lühr, H., Goncharenko, L. P., & Nagatsuma, T. (2010). Lunar-dependent equatorial ionospheric electrodynamic effects during sudden stratospheric warmings. *Journal of Geophysical Research*, *115*, 1–9. https://doi.org/10.1029/2010JA015273

Fenu, C., Reichel, L., & Rodriguez, G. (2016). GCV for Tikhonov regularization via global Golub-Kahan decomposition. *Numerical Linear Algebra with Applications*, *23*(3), 467–484. https://doi.org/10.1002/nla.2034

Fritts, D. C., & Alexander, M. J. (2003). Gravity wave dynamics and effects in the middle atmosphere. *Reviews of Geophysics*, *41*(1), 1003–1067. https://agupubs.onlinelibrary.wiley.com/doi/pdf/10.1029/2001RG000106

Goncharenko, L. P., Chau, J. L., Liu, H.-L., & Coster, A. J. (2010). Unexpected connections between the stratosphere and ionosphere. *Geophysical Research Letters*, *37*(10), 1–6. https://doi.org/10.1029/2010GL043125

Harding, B. J., Makela, J. J., Englert, C. R., Marr, K. D., Harlander, J. M., England, S. L., & Immel, T. J. (2017). The MIGHTI wind retrieval algorithm: Description and verification. *Space Science Reviews*, *212*, 585–600. https://doi.org/10.1007/s11214-017-0359-3

Harding, B. J., Makela, J. J., & Meriwether, J. W. (2015). Estimation of mesoscale thermospheric wind structure using a network of interferometers. *Journal of Geophysical Research: Space Physics*, *120*, 3928–3940. https://doi.org/10.1002/2015JA021025

He, M., & Chau, J. L. (2019). Mesospheric semidiurnal tides and near-12h waves through jointly analyzing observations of five specular meteor radars from three longitudinal sectors at boreal midlatitudes. *Atmospheric Chemistry and Physics*, *19*(9), 5993–6006. https://doi.org/10.5194/acp-19-5993-2019

He, M., Chau, J. L., Stober, G., Li, G., Ning, B., & Hoffmann, P. (2018). Relations between semidiurnal tidal variants through diagnosing the zonal wavenumber using a phase differencing technique based on two ground-based detectors. *Journal of Geophysical Research: Atmospheres*, *123*(8), 4015–4026. https://doi.org/10.1002/2018JD028400

Hocking, W. K. (2005). A new approach to momentum flux determinations using SKiYMET meteor radars. *Annales Geophysicae*, *23*(7), 2433–2439. https://doi.org/10.5194/angeo-23-2433-2005

Hocking, W. K. (2018). Spatial distribution of errors associated with multistatic meteor radar. *Earth, Planets and Space*, *70*(1), 93. https://doi.org/10.1186/s40623-018-0860-2

Hocking, W. K., Fuller, B., & Vandepeer, B. (2001). Real-time determination of meteor-related parameters utilizing modern digital technology. *Journal of Atmospheric and Solar-Terrestrial Physics*, *63*(2), 155–169.

Hoffmann, P., Singer, W., Keuer, D., Hocking, W. K., Kunze, M., & Murayama, Y. (2007). Latitudinal and longitudinal variability of mesospheric winds and temperatures during stratospheric warming events. *Journal of Atmospheric and Solar-Terrestrial Physics*, *69*, 2355–2366.

Holdsworth, D. A. (2005). Angle of arrival estimation for all-sky interferometric meteor radar systems. *Radio Science*, *40*, RS6010. https://doi.org/10.1029/2005RS003245

Holdsworth, D. A., Reid, I. M., & Cervera, M. A. (2004). Buckland Park all-sky interferometric meteor radar. *Radio Science*, *39*(5), RS5009. https://agupubs.onlinelibrary.wiley.com/doi/10.1029/2003RS003014

Huyghebaert, D., Hussey, G., Vierinen, J., McWilliams, K., & St-Maurice, J. P. (2019). ICEBEAR: An all-digital bistatic coded continuous-wave radar for studies of the E region of the ionosphere. *Radio Science*, *54*(4), 349–364. https://doi.org/10.1029/2018RS006747

Hysell, D. L., & Chau, J. L. (2002). Imaging radar observations and nonlocal theory of large-scale waves in the equatorial electrojet. *Annales Geophysicae*, *20*, 1167–1179.

Hysell, D. L., Larsen, M. F., & Sulzer, M. P. (2014). High time and height resolution neutral wind profile measurements across the mesosphere/lower thermosphere region using the Arecibo incoherent scatter radar. *Journal of Geophysical Research: Space Physics*, *119*(3), 2345–2358. https://doi.org/10.1002/(ISSN)2169-9402

Immel T. J., England S. L., Mende S. B., Heelis R. A., Englert C. R., Edelstein J., et al. (2018). The Ionospheric Connection Explorer Mission: Mission Goals and Design. *Space Science Reviews*, *214*(1), http://dx.doi.org/10.1007/s11214-017-0449-2

Immel, T. J., Sagawa, E., England, S. L., Henderson, S. B., Hagan, M. E., Mende, S. B., & Paxton, L. J. (2006). The control of equatorial ionospheric morphology by atmospheric tides. *Geophysical Research Letters*, *33*, L15108. https://doi.org/10.1029/2006GL026161

Jones, J., Webster, A. W., & Hocking, W. K. (1998). An improved interferometer design for use with meteor radars. *Radio Science*, *33*, 55–66.

Laskar, F. I., Chau, J. L., St.-Maurice, J. P., Stober, G., Hall, C. M., Tsutsumi, M., & Hoffmann, P. (2017). Experimental evidence of Arctic summer mesospheric upwelling and its connection to cold summer mesopause. *Geophysical Research Letters*, *44*(18), 9151–9158. https://doi.org/10.1002/2017GL074759

Lee, K., Kudeki, E., Reyes, P. M., Lehmacher, G. A., & Milla, M. (2019). Mesospheric wind estimation with the Jicamarca MST radar using spectral mainlobe identification. *Radio Science*, *54*(12), 1222–1239. https://doi.org/10.1029/2019RS006892

Manson, A. H., Meek, C. E., Chshyolkova, T., Xu, X., Aso, T., Drummond, J. R., & Ward, W. E. (2009). Arctic tidal characteristics at Eureka (80°N, 86°W) and Svalbard (78°N, 16°E) for 2006/07: Seasonal and longitudinal variations, migrating and non-migrating tides. *Annales Geophysicae*, *27*(3), 1153–1173. https://doi.org/10.5194/angeo-27-1153-2009

Meriwether, J., Faivre, M., Fesen, C., Sherwood, P., & Veliz, O. (2008). New results on equatorial thermospheric winds and the midnight temperature maximum. *Annales Geophysicae*, *26*, 447–466.

Murphy, D. J., Forbes, J. M., Walterscheid, R. L., Hagan, M. E., Avery, S. K., Aso, T., & Vincent, R. A. (2006). A climatology of tides in the Antarctic mesosphere and lower thermosphere. *Journal of Geophysical Research*, *111*, D23. https://doi.org/10.1029/2005JD006803

Nicolls, M. J., Cosgrove, R., & Bahcivan, H. (2014). Estimating the vector electric field using monostatic, multibeam incoherent scatter radar measurements. *Radio Science*, *49*(11), 1124–1139. https://doi.org/10.1002/2014RS005519

Oppenheim, M. M., Sugar, G., Slowey, N. O., Bass, E., Chau, J. L., & Close, S. (2009). Remote sensing lower thermosphere wind profiles using non-specular meteor echoes. *Geophysical Research Letters*, *36*(9), 1–5. https://doi.org/10.1029/2009GL037353

Pancheva, D., & Mukhtarov, P. (2011). Stratospheric warmings: The atmosphere-ionosphere coupling paradigm. *Journal of Atmospheric and Solar-Terrestrial Physics*, *73*(13), 1697–1702. https://doi.org/10.1016/j.jastp.2011.03.066

Pedatella, N. M., Chau, J. L., Schmidt, H., Goncharenko, L. P., Stolle, C., Hocke, K., & Siddiqui, T. A. (2018). How sudden stratospheric warming affects the whole atmosphere. *Eos*, *99*(6), 35–38. https://eos.org/features/how-sudden-stratospheric-warming-affects-the-whole-atmosphere

Pedatella, N. M., Liu, H.-L., Richmond, A. D., Maute, A., & Fang, T.-W. (2012). Simulations of solar and lunar tidal variability in the mesosphere and lower thermosphere during sudden stratosphere warmings and their influence on the low-latitude ionosphere. *Journal of Geophysical Research*, *117*, A08326. https://doi.org/10.1029/2012JA017858

Rajaram, R., & Gurubaran, S. (1998). Seasonal variabilities of low-latitude mesospheric winds. *Annales Geophysicae*, *16*(2), 197–204. https://doi.org/10.1007/s00585-998-0197-4

Rao, S. V. B., Eswaraiah, S., Venkat Ratnam, M., Kosalendra, E., Kishore Kumar, K., Sathish Kumar, S., & Gurubaran, S. (2014). Advanced meteor radar installed at Tirupati: System details and comparison with different radars. *Journal of Geophysical Research Atmospheres*, *119*(21), 11893–11904. https://agupubs.onlinelibrary.wiley.com/doi/10.1002/2014JD021781

Sandford, D. J., Muller, H. G., & Mitchell, N. J. (2006). Observations of lunar tides in the mesosphere and lower thermosphere at Arctic and middle latitudes. *Atmospheric Chemistry and Physics*, *6*(12), 4117–4127.

Shume, E. B., Hysell, D. L., & Chau, J. L. (2005). Zonal wind velocity profiles in the equatorial electrojet derived from phase velocities of type II radar echoes. *Journal of Geophysical Research*, *110*(A12), 8. https://doi.org/10.1029/2005JA011210

Smith, A. K. (2012). Global dynamics of the MLT. *Surveys in Geophysics*, *33*(6), 1177–1230. https://doi.org/10.1007/s10712-012-9196-9

Spargo, A. J., Reid, I. M., & MacKinnon, A. D. (2019). Multistatic meteor radar observations of gravity-wave tidal interaction over southern Australia. *Atmospheric Measurement Techniques*, *12*(9), 4791–4812. https://doi.org/10.5194/amt-12-4791-2019

Stober, G., & Chau, J. L. (2015). A multistatic and multifrequency novel approach for specular meteor radars to improve wind measurements in the MLT region. *Radio Science*, *50*(5), 431–442. https://doi.org/10.1002/2014RS005591

Stober, G., Chau, J. L., Vierinen, J., Jacobi, C., & Wilhelm, S. (2018). Retrieving horizontally resolved wind fields using multi-static meteor radar observations. *Atmospheric Measurement Techniques Discussions*, *2018*, 1–25. https://doi.org/10.5194/amt-2018-93

Tsutsumi, M., Holdsworth, D. A., Nakamura, T., & Reid, I. M. (1999). Meteor observations with an MF radar. *Earth, Planets and Space*, *51*, 691–699.

Urco, J. M., Chau, J. L., Milla, M. A., Vierinen, J. P., & Weber, T. (2018). Coherent MIMO to improve aperture synthesis radar imaging of field-aligned irregularities: First results at Jicamarca. *IEEE Transactions on Geoscience and Remote Sensing*, *99*, 1–11. https://doi.org/10.1109/TGRS.2017.2788425

Urco, J. M., Chau, J. L., Weber, T., Vierinen, J., & Volz, R. (2019). Sparse signal recovery in MIMO specular meteor radars with waveform diversity. *IEEE Transactions on Geoscience and Remote Sensing*, *57*(12), 10088–10098. https://ieeexplore.ieee.org/document/8802292

Vaudrin, C. V., Palo, S. E., & Chau, J. L. (2018). Complex plane specular meteor radar interferometry. *Radio Science*, *53*(1), 112–128. https://doi.org/10.1002/2017RS006317

Venkateswara Rao, N., Tsuda, T., & Kawatani, Y. (2012). A remarkable correlation between short period gravity waves and semiannual oscillation of the zonal wind in the equatorial mesopause region. *Annales Geophysicae*, *30*(4), 703–710. https://doi.org/10.5194/angeo-30-703-2012

Venkateswara Rao, N., Tsuda, T., Riggin, D. M., Gurubaran, S., Reid, I. M., & Vincent, R. A. (2012). Long-term variability of mean winds in the mesosphere and lower thermosphere at low latitudes. *Journal of Geophysical Research*, *117*, A10. https://doi.org/10.1029/2012JA017850

Vierinen, J., Chau, J. L., Charuvil, H., Urco, J. M., Clahsen, M., Avsarkisov, V., & Volz, R. (2019). Observing mesospheric turbulence with specular meteor radars: A novel method for estimating second-order statistics of wind velocity. *Earth and Space Science*, *6*(7), 1171–1195. https://doi.org/10.1029/2019EA000570

Vierinen, J., Chau, J. L., Pfeffer, N., Clahsen, M., & Stober, G. (2016). Coded continuous wave meteor radar. *Atmospheric Measurement Techniques*, *9*(2), 829–839. https://doi.org/10.5194/amt-9-829-2016

Vincent, R. A. (2015). The dynamics of the mesosphere and lower thermosphere: A brief review. *Progress in Earth and Planetary Science*, *2*(1), 4. https://doi.org/10.1186/s40645-015-0035-8

Waldteufel, P., & Corbin, H. (1979). On the analysis of single-Doppler radar data. *Journal of Applied Meteorology*, *18*(2), 532–542. https://doi.org/10.1175/1520-0450(1979)018⟨0532:OTAOSD⟩2.0.CO

Wallace, J. M., & Hobbs, P. V. (2006). *Atmospheric science: An introductory survey* (2nd ed.). Academic Press. https://doi.org/10.1016/C2009-0-00034-8. Retrieved from https://www.sciencedirect.com/book/9780127329512/atmospheric-science

Woodman, R. F., & Guillén, A. (1974). Radar observations of winds and turbulence in the stratosphere and mesosphere. *Journal of the Atmospheric Sciences*, *31*(2), 493–505.

Younger, J. P., & Reid, I. M. (2017). Interferometer angle-of-arrival determination using precalculated phases. *Radio Science*, *52*(9), 1058–1066. https://doi.org/10.1002/2017RS006284